International Journal for Numerical Methods in Engineering, Volume 117, Issue 9, March 2019

DOI: https://doi.org/10.1002/nme.5986

Received 11 October 2017; | Revised 11 October 2017; | Accepted 11 October 2017

DOI: xxx/xxxx

RESEARCH ARTICLE

Inverse Mass Matrix for Isogeometric Explicit Transient Analysis via the Method of Localized Lagrange Multipliers

José A. González[1] | J. Kopačka[2] | R. Kolman[2] | S.S. Cho[3] | K.C. Park[4]

[1]Escuela Técnica Superior de Ingeniería, Universidad de Sevilla, Camino de los Descubrimientos s/n, Seville E-41092, Spain

[2]Institute of Thermomechanics, The Czech Academy of Sciences, Dolejškova 5, 182 00 Prague, Czech Republic

[3]Reactor Mechanical Engineering Division, Korea Atomic Energy Research Institute, 999-111 Daedeok-Daero, Yuseong-gu, Daejeon 305-353, Republic of Korea

[4]Department of Aerospace Engineering Sciences, University of Colorado at Boulder, Boulder, CO 80309-429, USA

Correspondence
José A. González, Camino de los Descubrimientos s/n, Seville 41092, Spain.
Email: japerez@us.es

Present Address
Camino de los Descubrimientos s/n, Seville 41092, Spain

Abstract

A variational framework is employed to generate inverse mass matrices for isogeometric analysis. As different dual bases impact not only accuracy but also computational overhead, several dual bases are extensively investigated. Specifically, locally discontinuous bi-orthogonal basis functions are evaluated in detail for B-splines of high continuity and Bézier elements with a standard C^0 continuous finite element structure. The boundary conditions are enforced by the method of localized Lagrangian multipliers after generating the inverse mass matrix for completely free body. Thus, unlike inverse mass matrix methods without employing the method of Lagrange multipliers, no modifications in the reciprocal basis functions are needed to account for the boundary conditions. Hence, the present method does not require internal modifications of existing Isogeometric analysis software structures. Numerical examples show that globally continuous dual basis functions yield better accuracy than locally discontinuous bi-orthogonal functions, but with much higher computational overhead. Locally discontinuous dual basis functions are found to be an economical alternative to lumped mass matrices when combined with mass parametrization. The resulting inverse mass matrices are tested in several vibration problems and applied to explicit transient analysis of structures.

KEYWORDS:
Inverse mass matrix; isogeometric analysis; Bézier extraction; localized Lagrange multipliers; partitioned analysis; free vibration, explicit transient analysis

1 | INTRODUCTION

Efficient explicit time integration of structural dynamics equations calls for the availability of diagonal mass matrices. This is because the computational cost associated with the use of consistent/nondiagonal mass matrices in an explicit integration is equivalent with that of implicit time integration procedures, whose time step sizes can be chosen much larger than for explicit integration procedures. Specifically, explicit time integration methods in transient dynamics require a repeated application of the inverse mass matrix to obtain accelerations at every time step. For example, computing the inverse of a consistent mass matrix requires $\mathcal{O}(n^3)$ flops. This has led to the adoption of the diagonalized lumped mass matrix (LMM) that is typically obtained by a row-sum of the consistent mass matrix (CMM). However, even though the accuracy of LMM is acceptable for capturing low-frequency response components, it is unable to track high-frequency components[1,2,3,4,5]. Another shortcoming of LMM for higher-order elements is that most of the mass is lumped at the center node, causing very strange behavior when high-order

modes are excited. These deficiencies motivated researchers to find ways of generating the inverse of consistent mass matrix in a consistent and efficient way[6,7,8].

From the viewpoint of principles in dynamics, there are two ways for computing the mass matrices, which need to be inverted for efficient explicit time integration. One approach is to directly discretize system kinetic energy. The second is to exploit Hamilton's principle (or Hamilton's equations) that require discretization of both momentum ($\boldsymbol{p}$) and displacement ($\boldsymbol{u}$). In this case, the inverse mass matrix ($\mathbf{M}^{-1}$) is obtained as a second-order tensor product, where only a diagonalized projection operator ($\mathbf{A}$ which will be detailed later in the paper) needs to inverted, viz.:

$$\left(\int_{\Omega} \frac{1}{\rho}\delta\boldsymbol{p}\cdot\boldsymbol{p}\,d\Omega \approx \delta\mathbf{p}\,\mathbf{C}\,\mathbf{p}, \quad \int_{\Omega} \delta\boldsymbol{p}\cdot\boldsymbol{u}\,d\Omega \approx \delta\mathbf{p}\,\mathbf{A}^{\mathsf{T}}\,\mathbf{u}\right) \quad \Rightarrow \quad \mathbf{M}^{-1} = \mathbf{A}^{-\mathsf{T}}\mathbf{C}\mathbf{A}^{-1} \tag{1}$$

where $\mathbf{C}$ is labeled as a momentum matrix, $\mathbf{p}$ denotes discretized momentum vector. Hence, inversion of mass matrix is accomplished via the generation of the momentum matrix ($\mathbf{C}$) followed by a *push-forward* projection operation.

Thus, an efficient generation of consistent inverse mass matrices depends on how efficiently the projection operator ($\mathbf{A}$) can be generated and inverted. This in turn requires that the interpolation functions for the momentum must be bi-orthogonal with respect to the displacement interpolation functions so that the resulting projection matrix ($\mathbf{A}$) becomes diagonal. While derivations of bi-orthogonal basis functions are straightforward for most interpolation functions for the interior elements, for the elements bordering the boundaries, special bi-orthogonal basis functions need to be constructed. This construction has to performed for each of the corresponding $\mathbf{u}$-interpolation functions. It should be noted that, by the very nature of finite element method, elements bordering the boundaries do not need to be specialized.

The preceding complications in generating bi-orthogonal basis functions for the momentum vector in treating the boundary conditions were alleviated in the work of González et al.[9] for FEM by introducing the method of localized Lagrange multipliers[10,11,12,13]. In that work, the system is considered completely free floating such that no special treatment is required for generating the bi-orthogonal interpolation of the momentum vector. Enforcement of boundary conditions is simply accomplished via constraining the boundary conditions. We believe that the same ideas used for the obtention of FEM inverse mass matrices, can be extended to the more general framework of isogeometric analysis (IGA).

Particularly for IGA, different approaches have been proposed in the literature to address this difficulty present in the mass matrix inversion. First contributions in explicit dynamics were developed for B-spline collocation methods, treating the equations of motion (EOM) in strong form and obtaining one-point quadrature mass matrices[14,15]. Solutions to the mass inversion problem were then suggested at the time-integration solution algorithm level, introducing a *predictor multi-corrector* scheme that predicts accelerations with LMM on the left-hand-side of the linear system and corrects the residual using the CMM. This method is iterative in essence and energy stability is not guaranteed.

Other methods benefit from the regularity of the reference patches used in IGA, taking advantage of the tensor product separable form of the mass matrix associated to these structured meshes. For example, at the linear solver level with a CMM, Gao et al.[16] proposed using a *preconditioned conjugate gradient* method with special preconditioners that achieves a complexity of $\mathcal{O}(n)$ flops. However, this procedure is not completely general and non-separable mass matrices require a carefully designed preconditioner that adds significant complexity and computational cost to the linear solver. New preconditioning and multigrid techniques with linear cost[17,18,19] could also be considered for that task.

In the context of multi-patch discontinuous Galerkin IGA for acoustic wave propagation and linear advection, a recent work of Chan et al.[20] aims to approximate the mass matrix inverse by a computable *weight-adjusted mass matrix* that is pre-post multiplied by an easily invertible affine mass matrix obtained from the tensor product of 1D inverses. Although not derived from energy principles, the proposed algebraic approximation is demonstrated to be high order accurate only for sufficiently regular discretizations.

A different approach, the methodology used in this paper belongs to this last group, tries to derive a reciprocal mass matrix (RMM) directly from *parametrized variational principles* and dual-space shape functions[21]. The idea here is to derive variationally consistent reciprocal mass matrices from a parametrized functional and adjust the value of these parameters to construct customizable RMMs with desired properties, like high accuracy on certain frequency ranges or extending the critical time-step needed for time integration stability.

The objective of the present paper is to extend the procedure for generating FEM inverse mass matrices presented in González et al.[9] for explicit transient analysis by utilizing existing IGA capabilities[22,23,24,25]. To this end, the paper is organized as follows: Section 2 briefly reviews some basic concepts on B-splines, NURBS and Bézier elements interpolation. Section 3 derives the displacement-momentum mixed equations of elastodynamics from Hamilton's principle and Section 4 describes the direct

construction of inverse mass matrices through bi-orthogonal basis functions. Sections 5 and 6 categorize and analyze the construction of dual basis functions. Section 7 discusses the incorporation of boundary conditions into the inverse mass matrix via the method of localized Lagrange multipliers. Finally, in Section 8 we present several numerical examples, where we test the accuracy of the proposed mass matrix inverse in vibration and transient analyses, and Section 9 closes with the conclusions.

2 | A BRIEF REVIEW OF BASICS OF ISOGEOMETRIC ANALYSIS

In this Section we review the basic concepts of the isogeometric analysis techniques that will be used to construct the proposed reciprocal mass matrices. We start with the classical B-spline and NURBS approximation and next outline the basics of the Bézier extraction technique. This last technique is utilized to produce a finite element data structure of the geometry with the same approximation than the B-spline basis functions.

2.1 | B-splines and NURBS-based functions

In NURBS based Galerkin IGA, the approximation of a displacement field $\boldsymbol{u}(\mathbf{x})$ uses the same mathematical representation than the geometry based on spline-like approximation techniques[26]. For three-dimensional problems in particular, the geometry of a domain $\Omega \in \mathbb{R}^3$ is described by the tensor product formula:

$$\mathbf{x}(\xi,\eta,\zeta) = \sum_{i=1}^{n}\sum_{j=1}^{m}\sum_{k=1}^{l} R^{p,q,r}_{i,j,k}(\xi,\eta,\zeta)\,\mathbf{P}_{i,j,k}, \tag{2}$$

where $\mathbf{x} \in \Omega$ marks the position of point of interest in the physical space, (ξ,η,ζ) are its associated coordinates in the parametric space, $R^{p,q,r}_{i,j,k}$ are NURBS basis functions of orders (p,q,r) on each dimension, and $\mathbf{P}_{i,j,k}$ with $i = 1,\dots,n, j = 1,\dots,m, k = 1,\dots,l$ is a matrix with the three coordinates of the control points defining the geometry.

An associated displacement field $\boldsymbol{u}(\mathbf{x})$ is then approximated as follows:

$$\boldsymbol{u}(\mathbf{x}(\xi,\eta,\zeta)) = \sum_{i=1}^{n}\sum_{j=1}^{m}\sum_{k=1}^{l} R^{p,q,r}_{i,j,k}(\xi,\eta,\zeta)\,\mathbf{u}^{\mathrm{P}}_{i,j,k}, \tag{3}$$

where $\mathbf{u}^{\mathrm{P}}_{i,j,k}$ are now the displacements corresponding to the control point indicated by indices i,j,k.

For NURBS solids, the shape functions are described by the tensor product as

$$R^{p,q,r}_{i,j,k}(\xi,\eta,\zeta) = \frac{N^p_i(\xi)\,N^q_j(\eta)\,N^r_k(\zeta)\,w_{i,j,k}}{\sum_{\hat{i}=1}^{n}\sum_{\hat{j}=1}^{m}\sum_{\hat{k}=1}^{l} N^p_{\hat{i}}(\xi)\,N^q_{\hat{j}}(\eta)\,N^r_{\hat{k}}(\zeta)\,w_{\hat{i},\hat{j},\hat{k}}}, \tag{4}$$

where $w_{i,j,k}$ is referred to as the i,j,k-th *weight* corresponding to the i,j,k-th control point, and $N^p_i(\xi), N^q_j(\eta), N^r_k(\zeta)$ are univariate B-spline basis functions of orders p, q and r corresponding to the knot vectors Ξ, $\mathcal{H}$, $\mathcal{Z}$, respectively[27].

Let us define a knot vector in one-dimensional case as a non-decreasing set of coordinates in the parametric space, written as $\Xi = \{\xi_1,\xi_2,\dots,\xi_{m_k}\}$, where $\xi_i \in \mathbb{R}$ is the i-th knot, i is the knot index, $i = 1,2,\dots,m_k$, number of knots $m_k = n + p + 1$, order p is the polynomial degree and n is the number of basis functions (control points) used to construct the B-spline curve. Associated B-spline basis functions $N^p_i(\xi)$, see Figure 1, are C^{p-k} continuous piecewise polynomials defined by the Cox-de Boor recursion formula[28]. Observe that N^p_i are C^{p-k} continuous piecewise polynomials, where k is the knot multiplicity, and that continuity can be controlled by the multiplicity of a knot in the knot vector Ξ.

Finally, the NURBS based interpolation in $\mathbb{R}^3$ of a displacement field $\boldsymbol{u}(\mathbf{x})$ can then be expressed in matrix form as:

$$\boldsymbol{u}(\boldsymbol{\xi}) = \sum_{i=1}^{n} \mathbf{N}^p_i(\boldsymbol{\xi})\,\mathbf{u}^{\mathrm{P}}_i = \mathbf{N}_u(\boldsymbol{\xi})\,\mathbf{u}, \tag{5}$$

where the matrix of interpolation functions $\mathbf{N}_u(\boldsymbol{\xi})$ is constructed by using B-spline basis functions of a given degree p and vector $\mathbf{u}$ groups the unknown discrete values at the control points.

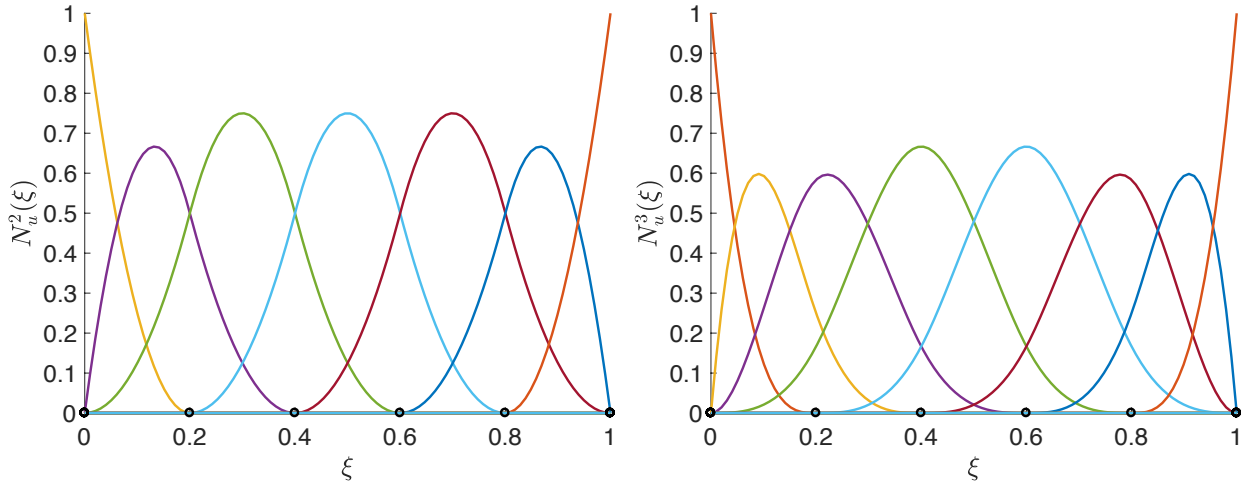

FIGURE 1 Standard one-dimensional quadratic p=2 (left) and cubic p=3 (right) B-spline basis functions $N_u^p(\xi)$ in the normalized parameter space for an open knot vector with internal values $\Xi = \{0, 0.2, 0.4, 0.6, 0.8, 1\}$.

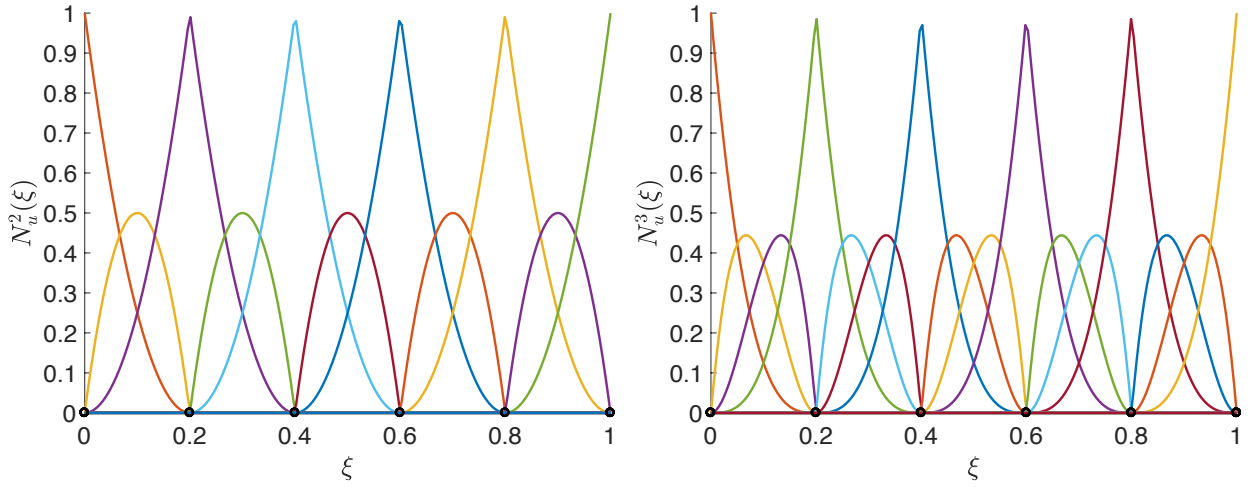

FIGURE 2 Result of the application of the Bézier extraction process to the original quadratic p=2 (left) and cubic p=3 (right) B-spline basis functions represented in Figure 1. After knot insertion, $\Xi = \{0, 0.2, 0.2, 0.4, 0.4, 0.6, 0.6, 0.8, 0.8, 1\}$ for $p = 2$, the original B-spline basis functions can be expressed as a linear combination of the new Bézier interpolation functions with compact support.

2.2 | Bézier extraction - transformation of NURBS based mesh into Bézier based mesh

As mentioned in the previous section, the support of a B-spline basis function N_i^p is compact and contained over $p+1$ knot spans in the interval $[\xi_i, \xi_{i+p+1}]$. As a result, it is not possible to use the concept of a single parent finite element with locally defined shape functions that is mapped onto individual knot intervals, complicating the implementation. One solution to circumvent this difficulty is the Bézier's extraction process[29].

In the same way that NURBS are a generalization of B-Splines, B-Splines rerpesent the generalization of Bézier splines (based on Bernstein polynomials) and as such, the Bézier representation of a domain can be written in the form:

$$\mathbf{x}(\xi, \eta, \zeta) = \sum_{i=1}^{n} \sum_{j=1}^{m} \sum_{k=1}^{l} B_{i,j,k}^{p,q,r}(\xi, \eta, \zeta)\, \mathbf{P}_{i,j,k}^{B} \tag{6}$$

where $\mathbf{P}_{i,j,k}^{B}$ are new coordinates of control points for a Bézier based representation and $B_{i,j,k}^{p,q,r}$ are the shape functions based on the Bernstein polynomials of order p, q, r.

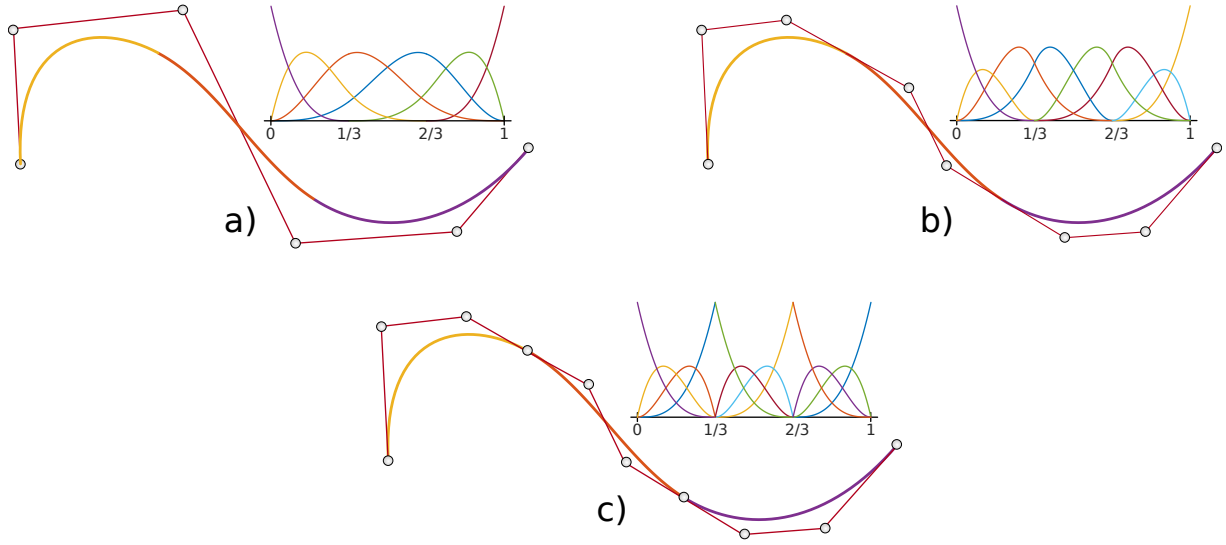

FIGURE 3 Bézier extraction operation performed in a 2D cubic ($p = 3$) B-spline curve. The shape of the initial C^2 continuous curve (a) is defined by six control points and six basis functions, and its associated knot vector is $\Xi = \{0,0,0,0,1/3,2/3,1,1,1,1\}$. After a first repetition of knot values, one gets the curve with C^1 continuity (b) with eight control points/basis functions and knot vector $\Xi = \{0,0,0,0,1/3,1/3,2/3,2/3,1,1,1,1\}$. Finally, p repetitions of the knot values results in the C^0 continuous curve (c) with ten control points/basis functions and knot vector $\Xi = \{0,0,0,0,1/3,1/3,1/3,2/3,2/3,2/3,1,1,1,1\}$. Now the basis functions are the same for all the knot intervals, therefore the curve can be constructed through a systematic assembling of Bézier elements with Bernstein polynomials as shape functions.

By Bézier extraction, it is meant the construction of a mesh of isogeometric Bézier elements from a NURBS representation. This process provides a local element support structure for isogeometric analysis, that can be easily incorporated into existing finite element codes, see Figure 3. Following this technique, the B-spline functions $\mathbf{N}(\boldsymbol{\xi})$ can be unambiguously written as linear combination of Bernstein polynomials $\mathbf{B}(\boldsymbol{\xi})$, expressed in matrix form:

$$\mathbf{N}(\boldsymbol{\xi}) = \mathbf{C}_B \mathbf{B}(\boldsymbol{\xi}), \tag{7}$$

where matrix $\mathbf{C}_B$ is the extraction operator, that is uniquely associated to a particular knot vector[29].

Technically, the new mesh is constructed step-by-step repeating all the knots contained in the original knot vector up to multiplicity $p+1$, reducing at the same time continuity to C^0, by following the process described in Figure 3. Then, for each B-spline segment, an expression like (7) can be expressed in local form. Furthermore, new position and weights of the Bézier mesh, $\mathbf{P}^B$ and $\mathbf{w}_B$, can be computed directly from the position of control points and weights, $\mathbf{P}$ and $\mathbf{w}$, corresponding to the NURBS mesh as:

$$\mathbf{P}^B = \mathbf{W}_B^{-1}\mathbf{C}_B^{\mathsf{T}}\mathbf{W}\mathbf{P}, \qquad \mathbf{w}_B = \mathbf{C}_B^{\mathsf{T}}\mathbf{w}, \tag{8}$$

where matrices $\mathbf{W}_B$ and $\mathbf{W}$ are diagonal matrices storing the weight vectors $\mathbf{w}^b$ and $\mathbf{w}$, for more details see[29].

In a typical 2D case, like the one represented in Figure 4, Bézier analysis starts with an IGA mesh. Then, one can use the previous transformations to convert step-by-step the NURBS based mesh into a Bézier mesh by repeating knots in the two parametric directions. Finally, a finite element mesh is obtained with C^0 continuity of neighboring elements with Bernstein polynomials as shape functions.

3 | HAMILTON'S PRINCIPLE WITH THE METHOD OF LOCALIZED LAGRANGE MULTIPLIERS

We consider the evolution in time of the displacement and momentum fields $\boldsymbol{u}, \boldsymbol{p} \in \mathbb{R}^d$, where $d = 1,2,3$ is the number of space dimensions, of a body with domain Ω and boundary Γ for a total time T. The body is subjected to prescribed interface displacements $\boldsymbol{u}_b$ on part of its boundary Γ_b, to the traction $\boldsymbol{t}$ on the rest of its boundary Γ_t and to a body force $\boldsymbol{b}$ per unit volume.

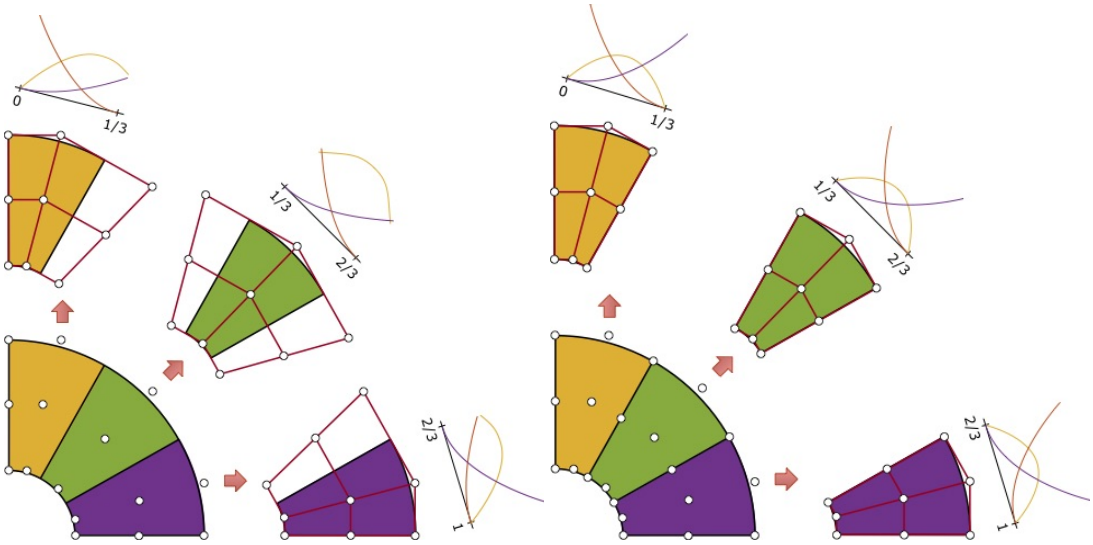

FIGURE 4 Illustration of the Bézier extraction operation performed in a 2D patch of quadratic B-splines. The Bézier extraction operator maps a piecewise Bernstein polynomials basis (right) onto a B-spline basis (left). This transformation makes it possible to create Bézier elements as the finite element representation of B-splines or NURBS.

Initial conditions that are compatible with the boundary conditions define the displacement and velocity field respectively at time $t = 0$. The initial boundary value problem of elastodynamics expressed in strong form can be formulated as follows:

$$\begin{aligned} \boldsymbol{\nabla} \cdot \boldsymbol{\sigma} + \boldsymbol{b} = \dot{\boldsymbol{p}} \quad & \text{in} \quad \Omega \times [0,T]\,, \\ \boldsymbol{u} = \boldsymbol{u}_b \quad & \text{on} \quad \Gamma_b \times [0,T]\,, \\ \boldsymbol{\sigma} \cdot \boldsymbol{n} = \boldsymbol{t} \quad & \text{on} \quad \Gamma_t \times [0,T]\,, \\ \boldsymbol{u}|_{t=0} = \boldsymbol{u}^0 \quad & \text{in} \quad \Omega, \\ \dot{\boldsymbol{u}}|_{t=0} = \dot{\boldsymbol{u}}^0 \quad & \text{in} \quad \Omega, \end{aligned} \tag{9}$$

where $\boldsymbol{p} = \rho\dot{\boldsymbol{u}}$ is the momentum per unit volume and $\boldsymbol{\sigma}$ is the stress tensor that, in the case of linear elasticity is linearly related with the deformation tensor $\boldsymbol{\varepsilon} = \frac{1}{2}[\nabla\boldsymbol{u} + \nabla^{\mathsf{T}}\boldsymbol{u}]$ by the fourth-order constitutive tensor $\boldsymbol{C}$ through the constitutive relation $\boldsymbol{\sigma} = \boldsymbol{C} : \boldsymbol{\varepsilon}$. This is an initial value problem to be solved for all time t in the interval $[0, T]$.

The strong form of the of the initial value problem (9) can be transformed into an equivalent weak variational form. To this end, we invoke Hamilton's principle for constrained elastodynamic problems. This principle states that *the path followed by a dynamic system is the one which minimizes the action integral of the Lagrangian*; condition that can be expressed using the following three-field variational form:

$$\delta H(\boldsymbol{u}, \boldsymbol{p}, \boldsymbol{\ell}) = \int_{t_1}^{t_2} \delta \left\{ T(\dot{\boldsymbol{u}}, \boldsymbol{p}) - U(\boldsymbol{u}, \boldsymbol{\ell}) + W(\boldsymbol{u}) \right\} \, dt = 0, \tag{10}$$

where δT is the virtual kinetic energy, δU the virtual elastic energy and δW the virtual work done by the external loads, magnitudes that can be expressed:

$$\delta T = \int_{\Omega} \delta(\tfrac{1}{2}\boldsymbol{p} \cdot \dot{\boldsymbol{u}}) \, d\Omega, \tag{11}$$

$$\delta U = \int_{\Omega} \delta\boldsymbol{\varepsilon} : \boldsymbol{\sigma} \, d\Omega + \int_{\Gamma_b} \delta \left\{ \boldsymbol{\ell} \cdot (\boldsymbol{u} - \boldsymbol{u}_b) \right\} \, d\Gamma, \tag{12}$$

$$\delta W = \int_{\Omega} \delta\boldsymbol{u} \cdot \boldsymbol{b} \, d\Omega, \tag{13}$$

with known displacement boundary conditions $\boldsymbol{u}_b$ imposed at interface Γ by using a field of localized Lagrange multipliers $\boldsymbol{\ell}$ and external body forces per unit volume $\boldsymbol{b}$ acting on Ω.

By making use of the momentum-velocity relation ($\boldsymbol{p} = \rho\dot{\boldsymbol{u}}$) in the following identity:

$$\tfrac{1}{2}\boldsymbol{p}\cdot\dot{\boldsymbol{u}} = \boldsymbol{p}\cdot\dot{\boldsymbol{u}} - \tfrac{1}{2\rho}\boldsymbol{p}\cdot\boldsymbol{p} \tag{14}$$

we can obtain an equivalent expression for the virtual kinetic energy per unit volume:

$$\delta\left(\tfrac{1}{2}\boldsymbol{p}\cdot\dot{\boldsymbol{u}}\right) = \delta\dot{\boldsymbol{u}}\cdot\boldsymbol{p} + \delta\boldsymbol{p}\cdot\left(\dot{\boldsymbol{u}} - \tfrac{1}{\rho}\boldsymbol{p}\right) \tag{15}$$

and finally performing an integration by parts of the second term of the last equation yields:

$$\int_{t_1}^{t_2} \delta\dot{\mathbf{u}}\cdot\boldsymbol{p}\,dt = -\int_{t_1}^{t_2} \delta\boldsymbol{u}\cdot\dot{\boldsymbol{p}}\,dt, \tag{16}$$

relation that can be used to eliminate the virtual velocity field from the formulation.

Introducing previous identities, (15) and (16), into the principle of stationary action (10), we obtain the final the three-field variational form of the Hamilton's principle for constrained elastodynamics:

$$\delta H(\boldsymbol{u},\boldsymbol{p},\boldsymbol{\ell}) = \int_{t_1}^{t_2}\left\{\int_\Omega \delta\boldsymbol{p}\cdot\left(\dot{\boldsymbol{u}} - \tfrac{1}{\rho}\boldsymbol{p}\right)\,d\Omega - \int_\Omega (\delta\boldsymbol{u}\cdot\dot{\boldsymbol{p}} + \delta\boldsymbol{\varepsilon} : \boldsymbol{\sigma})\,d\Omega + \int_\Omega \delta\boldsymbol{u}\cdot\boldsymbol{b}\,d\Omega \right.$$
$$\left. + \int_{\Gamma_b} \delta\boldsymbol{u}\cdot\boldsymbol{\ell}\,d\Gamma - \int_{\Gamma_b} \delta\boldsymbol{\ell}\cdot\left(\boldsymbol{u} - \boldsymbol{u}_b\right)\,d\Gamma\right\} dt = 0, \tag{17}$$

expression that will be used to derive the discrete equations of motion.

Remark 1. Through the use of a parametrized form of the kinematic energy with three free parameters $\left(C_1, C_2, C_3\right)$, Schaeuble et al.[21] proposed a general template for obtaining variationally scaled and customized consistent and reciprocal mass matrices. Variational equation (17) can be considered a particular case of their general template form for $\left\{C_1 = -1, C_2 = 0, C_3 = 0\right\}$. An important difference with that work lies on the use of a volume-specific linear momentum instead of a mass-specific linear momentum and the consistent-lumped parametrization of the mass matrix that will be introduced later.

4 | CONSTRUCTING INVERSE MASS MATRIX VIA THE LOCALIZED LAGRANGE MULTIPLIERS

Discretization in space of the mixed variational form (17) is performed by using independent interpolation functions for displacements, momenta and Lagrangian multipliers. For this purpose, we carry out a standard IGA discretization (5) with independent B-spline shape functions for the three fields:

$$\boldsymbol{u}(\boldsymbol{\xi}) = \mathbf{N}_u(\boldsymbol{\xi})\,\mathbf{u}, \qquad \boldsymbol{p}(\boldsymbol{\xi}) = \mathbf{N}_p(\boldsymbol{\xi})\,\mathbf{p}, \qquad \boldsymbol{\ell}(\boldsymbol{\xi}) = \mathbf{N}_\lambda(\boldsymbol{\xi})\,\boldsymbol{\lambda}, \tag{18}$$

and introduce these discrete approximations in the variational form (17) to obtain, after imposing the stationarity condition, the following set of semi-discrete equations:

$$\mathbf{A}\dot{\mathbf{p}} + \mathbf{B}\boldsymbol{\lambda} = \mathbf{r} \qquad \textit{Equilibrium equation}, \tag{19}$$
$$\mathbf{A}^{\mathsf{T}}\dot{\mathbf{u}} - \mathbf{C}\mathbf{p} = \mathbf{0} \qquad \textit{Momentum equation}, \tag{20}$$
$$\mathbf{B}^{\mathsf{T}}\mathbf{u} - \mathbf{L}_b\mathbf{u}_b = \mathbf{0} \qquad \textit{Boundary (and interface) constraints}, \tag{21}$$
$$-\mathbf{L}_b^{\mathsf{T}}\boldsymbol{\lambda} = \mathbf{0} \qquad \textit{Newton's 3rd law on the boundaries}, \tag{22}$$

where vector $\mathbf{r} = \mathbf{f} - \mathbf{f}^{int}$ is the external-internal forces residual, $\mathbf{A}$ is the global projection matrix, $\mathbf{C}$ the global reciprocal mass matrix, $\mathbf{B}$ the boundary assembly operator and $\mathbf{L}_b$ the Localized multipliers assembly matrix. These matrices are constituted by

an element-by-element assembly of the element matrices:

$$\mathbf{A}_e = \int_{\Omega_e} \mathbf{N}_u^{\mathsf{T}}\, \mathbf{N}_p \, d\Omega\,, \qquad \mathbf{C}_e = \int_{\Omega_e} \tfrac{1}{\rho}\mathbf{N}_p^{\mathsf{T}}\, \mathbf{N}_p \, d\Omega, \tag{23}$$

$$\mathbf{B}_e = \int_{\Gamma_e} \mathbf{N}_u^{\mathsf{T}}\, \mathbf{N}_\lambda \, d\Gamma\,, \qquad \mathbf{L}_e = \int_{\Gamma_e} \mathbf{N}_\lambda^{\mathsf{T}}\, \mathbf{N}_u \, d\Gamma, \tag{24}$$

the first two needed for the construction of the element reciprocal mass and the last ones used to enforce interface compatibility and equilibrium. Moreover it is important to mention that we assume constant mass density along every physical patch.

Going one step forward by eliminating symbolically the momentum variable $\mathbf{p}$ from (19) and (20), one obtains the classical equation of motion expressed in terms of displacements:

$$\left(\mathbf{A}\mathbf{C}^{-1}\mathbf{A}^{\mathsf{T}}\right)\ddot{\mathbf{u}} + \mathbf{B}\boldsymbol{\lambda} = \mathbf{r} \tag{25}$$

with the mass matrix approximated as:

$$\mathbf{M} = \mathbf{A}\mathbf{C}^{-1}\mathbf{A}^{\mathsf{T}} \tag{26}$$

and observe that there must exist an inverse mass matrix (denoted by equivalence as $\mathbf{M}^{-1}$) given by:

$$\mathbf{M}^{-1} = \mathbf{A}^{-\mathsf{T}}\mathbf{C}\mathbf{A}^{-1} \tag{27}$$

assuming that the global projection matrix is invertible.

Since the objective of the present paper is to obtain inverse mass-matrices for IGA in efficient and accurate ways, one must seek for easily to invert *diagonal* or narrowly banded projection matrices. This certainly can be accomplished in (27) with a diagonal projection $\mathbf{A}$-matrix, leaving only the task of constructing the reciprocal $\mathbf{C}$-matrix efficiently and accurately.

5 | DUAL BASIS FUNCTIONS

Observing again the expression obtained for the mass matrix inverse (27), we realize that a careful selection of the basis functions can simplify its calculation. Dual bases can be *local* or *global*, *continuous* or *discontinuous* and satisfy exactly the orthogonality condition or not. In particular, by using displacement and momentum bi-orthogonal interpolation functions, we are able to construct a diagonal projection matrix in the form:

$$\left[\mathbf{A}_e\right]_{ij} = \int_{\Omega_e} \mathbf{N}_{u_i}^{\mathsf{T}}\mathbf{N}_{p_j}\, d\Omega = d_i\delta_{ij}, \quad \text{where } \left[\mathbf{A}_e\right]_{ij} = 0 \text{ for } i \neq j \tag{28}$$

with a trivial inverse that permits to compute the inverse mass matrix directly from the momentum matrix. Different local and global dual interpolation functions of this kind, originally designed and tested for mortar methods, have been recently proposed in the literature[30,31,32] for NURBS and B-spline interpolations. Specifically for the construction of reciprocal mass matrices, bi-orthogonal basis functions have been proposed under the framework of FEM[8,9] and also IGA[21]. The different options available for the construction of dual bases are discussed next.

5.1 | Local dual bases

These dual basis functions entail minimal support, i.e., the support of the dual basis is equal to the support of the original B-spline basis, that for the case of B-splines covers $p+1$ knot spans. Analytical expressions for the construction of local continuous (LC) bi-orthogonal dual basis exist in the literature for one-dimensional B-splines[33,34,32], but they are difficult to generalize for multidimensions, restricting their application to our case.

For higher dimensions, the simplest alternative is the use of a local discontinuous (LD) bi-orthogonal dual basis[35,31] obtained via an element-wise linear combination of the primal shape functions, providing discontinuous reciprocal basis functions that fulfill the partition of unity with the same support than their primal counterparts. A dual basis $\mathbf{N}_p(\boldsymbol{\xi})$ of this type, orthogonal to the B-spline displacement interpolation functions $\mathbf{N}_u(\boldsymbol{\xi})$, can be written in matrix form as:

$$\mathbf{N}_p(\boldsymbol{\xi}) = \mathbf{N}_u(\boldsymbol{\xi})\mathbf{M}_e^{-1}\mathbf{M}_e^L \tag{29}$$

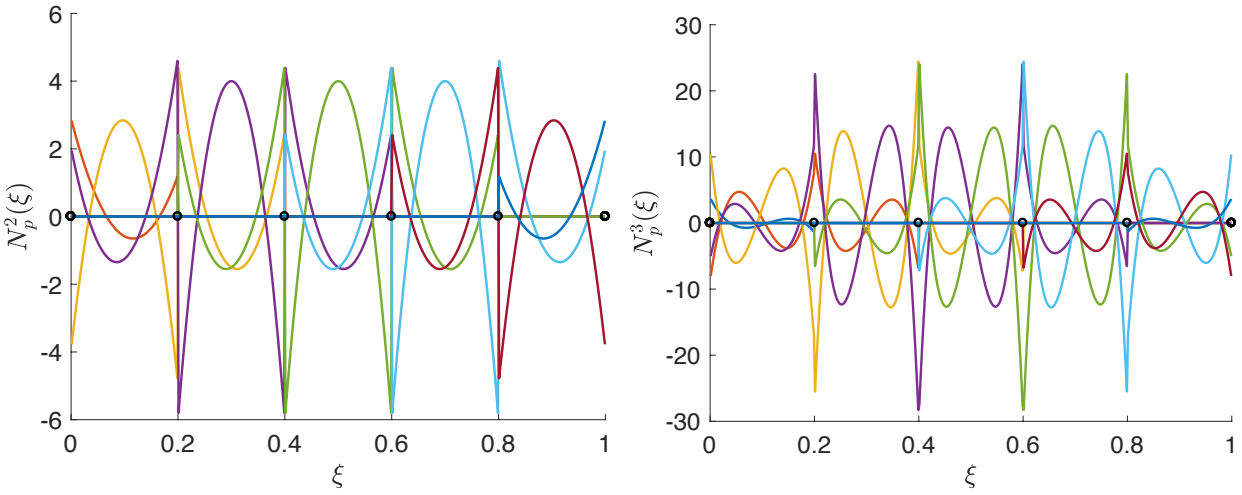

FIGURE 5 Representation of local discontinuous quadratic p=2 (left) and cubic p=3 (right) orthogonal B-spline basis functions $N_p^p(\xi)$ in the normalized parameter space for an open knot vector with internal values $\Xi = \{0, 0.2, 0.4, 0.6, 0.8, 1\}$. These dual interpolation functions are locally orthogonal to the basis $N_u^p(\xi)$ represented in Figure 1 .

constructed by using the knot intervals as independent elements and where $\mathbf{M}_e$ is an element-by-element constructed mass matrix, with $\mathbf{M}_e^L = \mathbf{diag}\left(\sum_j \left[\mathbf{M}_e\right]_{ij}\right)$ the lumped mass matrix obtained by row-sum of its components.

Orthogonality of these interpolation functions is easily demonstrated evaluating the projection matrix (28) at the element level:

$$\mathbf{A}_e = \int_{\Omega_e} \mathbf{N}_u^\mathsf{T} \mathbf{N}_p \, d\Omega = \{ \int_{\Omega_e} \mathbf{N}_u^\mathsf{T} \mathbf{N}_u \, d\Omega \} \, \mathbf{M}_e^{-1} \mathbf{M}_e^L = \frac{1}{\rho} \mathbf{M}_e^L \tag{30}$$

obtaining by design a diagonal projection matrix $\mathbf{A}_e$ that is equal to the lumped element mass matrix computed with unit density. As an example, Figure 5 represents the discontinuous interpolation functions $N_p^p(\xi)$ locally orthogonal to the B-spline basis $N_u^p(\xi)$ contained in Figure 1 for quadratic (p=2) and cubic (p=3) B-spline interpolations.

Finally, we can evaluate analytically the elemental momentum mass matrix from its definition (23), by substituting (29) and considering (30), with a very simple expression:

$$\mathbf{C}_e = \int_{\Omega_e} \frac{1}{\rho} \mathbf{N}_p^\mathsf{T} \mathbf{N}_p \, d\Omega = \mathbf{A}_e^\mathsf{T} \mathbf{M}_e^{-1} \mathbf{A}_e \tag{31}$$

confirming that it is possible to compute a reciprocal mass matrix element-by-element without expensive operations.

Remark 2. Expression (30), with the element projection matrix $\mathbf{A}_e$ equal to the lumped element mass matrix, was originally proposed by González et al.[9] for the construction of reciprocal mass matrices in the context of FEM. The same projection matrix was later employed by Schaeuble et al.[21] to construct variationally consistent masses and reciprocal masses for IGA, eliminating the density inverse from its definition by introducing a momentum velocity field instead of a pure momentum field.

A similar element-wise construction process can be applied to Bézier elements, obtaining a basis with compact support restricted to the knot intervals that presents C^0 continuity at the element interfaces. In this case, see Figure 6 , the local dual basis presents the same support than the original basis and the element-by-element compact support is well defined.

5.2 | Global dual bases

On the contrary, global dual basis functions present complete support along the parametric space. A common technique to compute global continuous (GC) bases is to write the dual functions as linear combination of the primal shape functions, finding the coefficients by enforcing the orthogonality condition. Accelerated algorithms[36] exist for this task, exploiting the mathematical properties of the dual bases that can reduce the algorithm complexity, from $\mathcal{O}(n^3)$ flops needed to compute a full inverse, to $\mathcal{O}(n^2)$ flops.

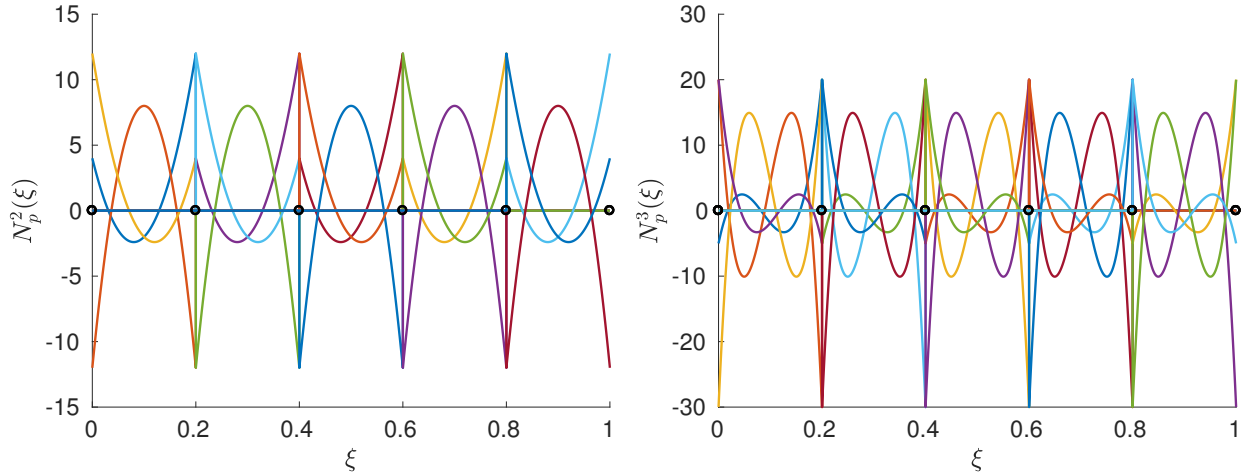

FIGURE 6 Form of the quadratic p=2 (left) and cubic p=3 (right) local discontinuous dual basis functions $N_p(\xi)$ locally orthogonal to the Bézier element basis $N_u^p(\xi)$ represented in Figure 2.

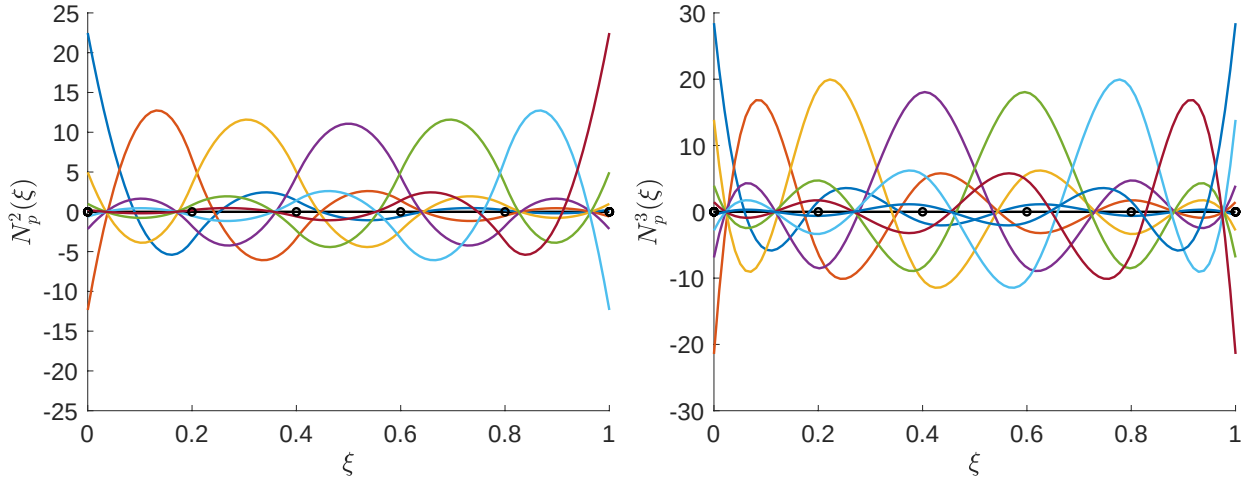

FIGURE 7 Representation of quadratic p=2 (left) and cubic p=3 (right) B-spline global continuous dual basis functions $N_p^p(\xi)$ in the normalized parameter space for an open knot vector with internal values $\Xi = \{0, 0.2, 0.4, 0.6, 0.8, 1\}$. These interpolation functions are orthogonal to the basis $N_u^p(\xi)$ represented in Figure 1.

Another possibility to determine GC dual basis functions for B-spline basis functions is the inversion of the *Gram* matrix[32,37]. In this case, the first step in the calculation of the dual basis requires the computation of the Gramian matrix for the primal basis:

$$\mathbf{G}_{N_u,N_u} = \left[\int_{\xi_1}^{\xi_{n+p+1}} N_{u_i}(\xi) N_{u_j}(\xi)\, ds \right]_{(i=1,\ldots,n;\ j=1,\ldots,n)} \tag{32}$$

that integrates cross products of primal B-spline functions along the complete parametric space. The resulting Gram matrix is symmetric, block-diagonal and always invertible. Then, the Gram matrix needs to be efficiently inverted to obtain the dual basis:

$$\mathbf{N}_p(\boldsymbol{\xi}) = \mathbf{G}_{N_u,N_u}^{-1} \mathbf{N}_u(\boldsymbol{\xi}) \tag{33}$$

where a full populated inverse $\mathbf{G}_{N_u,N_u}^{-1}$ produces a dual basis with global support. The resulting GC bi-orthogonal basis functions yield the optimal reproduction degree, but increase the number of operations and storage needed to compute the inverse mass matrix due to their full support, see Figure 7.

Compared to local reciprocal bases, global dual basis functions produce full reciprocal mass matrices that are computationally more expensive. In particular, the RMM computed with the inverse of the *Gram* dual basis (33) yields very accurate numerical results, but at significantly higher computational cost than local dual bases.

5.3 | Convenient dual bases

We incorporate into this final category bases that are not strictly orthogonal but can simplify the computation of the mass inverse thanks to the exploitation of a convenient property. One example is the *approximate dual basis* based on wavelets proposed in Dornisch et al.[32] for mortar coupling methods, that are able to produce semi-compact approximations of an orthogonal basis.

Another example is the inverse mass matrix approximation proposed by Chan et al.[20], in the context of discontinuous Galerkin IGA for wave propagation, where an approximated *weight-adjusted* reciprocal mass matrix is derived empirically. It is interesting to note that the same inverse mass matrix is obtained if we apply the proposed variational framework to the LC ansatz basis,

$$\mathbf{N}_p(\boldsymbol{\xi}) = \mathbf{N}_u(\boldsymbol{\xi}) J^{-1}(\boldsymbol{\xi}), \tag{34}$$

where $J(\boldsymbol{\xi})$ is the Jacobian determinant of the physical to parametrical domain transformation and $\hat{\Omega}$ represents the parametric domain. This basis is not bi-orthogonal, but a simple scaling of the primal basis and its advantage resides in the elimination of the physical domain influence from the projection matrix (23),

$$\mathbf{A} = \int_{\Omega} \mathbf{N}_u^{\mathsf{T}} \mathbf{N}_p \, d\Omega = \int_{\hat{\Omega}} \mathbf{N}_u^{\mathsf{T}} \mathbf{N}_u \, d\hat{\Omega} = \mathbf{M}_{\hat{\Omega}} \tag{35}$$

a mass matrix that is not diagonal, but is constant for a particular patch and its inversion can be automatized for regular structured patches or affine transformations. The associated momentum matrix is then computed as,

$$\mathbf{C} = \int_{\Omega} \mathbf{N}_u^{\mathsf{T}} \mathbf{N}_u J^{-1}(\boldsymbol{\xi}) \, d\Omega \tag{36}$$

and from (27) the inverse mass matrix presents the form,

$$\mathbf{M}^{-1} = \mathbf{M}_{\hat{\Omega}}^{-1} \mathbf{C} \mathbf{M}_{\hat{\Omega}}^{-1}, \tag{37}$$

where the mass inverse of the parametric domain can be written as the tensor product,

$$\mathbf{M}_{\hat{\Omega}}^{-1} = \mathbf{M}_{1D}^{-1} \otimes \cdots \otimes \mathbf{M}_{1D}^{-1}, \tag{38}$$

when the parametric domain $\hat{\Omega}$ is regular with the same structure on each dimension. In this specific case, the inverse mass matrix in one direction $\mathbf{M}_{1D}^{-1}$ is very cheap to compute and the complete patch inverse presents a Kronecker delta structure.

6 | ASSESSMENT OF LOCAL DISCONTINUOUS DUAL BASES

From all the possible dual basis functions discussed in Section 5, the element-wise computation of a LD bi-orthogonal basis seems a perfect candidate, due to its simplicity and good results demonstrated in FEM and IGA mortar methods. LD bi-orthogonal bases produce diagonal projection matrices and sparse inverse mass matrices. In this Section we describe in detail its implementation and integration into the proposed variational framework. It is also performed a dispersion study that reveals the weakness of this type of basis under certain conditions, together with a parametrization method of the mass matrix that palliates this defect.

6.1 | Procedure to obtain IGA reciprocal mass matrices

The procedure used for the evaluation of the inverse mass matrix for IGA can be summarized in the following steps:

1. Consider all the open patches independently as free-floating substructres.
2. Compute element by element a parametrized mass matrix $\mathbf{M}_e$ using (43) for example.
3. Approximate the element projection matrix $\mathbf{A}_e$ by lumping the element mass matrix.

4. Compute the element reciprocal mass matrix $\mathbf{C}_e$ from a direct inversion of the element mass matrix.
5. Assemble the global projection and reciprocal matrices and compute the global mass matrix inverse.
6. Impose boundary conditions between patches using localized Lagrange multipliers.

The first four steps of this process are described next and the last step, that is a little bit more involved, will be analyzed in Section 7.

First, we consider an element of the patch at a time and compute the parametrized element mass matrix. Second, we use the element lumped mass matrix to obtain the element projection matrix by diagonalization, viz.:

$$\mathbf{A}_e = \frac{1}{\rho}\mathbf{M}_e^L \tag{39}$$

assuming that the density is constant in the patch. Third, the elemental reciprocal mass matrix is evaluated inverting numerically the element mass matrix:

$$\mathbf{C}_e = \mathbf{A}_e^{\mathsf{T}}\mathbf{M}_e^{-1}\mathbf{A}_e \tag{40}$$

where $(\mathbf{A}_e, \mathbf{C}_e, \mathbf{M}_e)$ are elemental matrices, and particularly $\mathbf{A}_e$ is a diagonal matrix, so this operation is very cheap.

Finally, we proceed with the assembly of the global reciprocal mass matrix:

$$\mathbf{C} = \mathop{\mathsf{A}}_{e=1}^{N_e} \mathbf{C}_e \tag{41}$$

and the global projection matrix:

$$\mathbf{A} = \mathop{\mathsf{A}}_{e=1}^{N_e} \mathbf{A}_e \tag{42}$$

observing that as long as the elemental $\mathbf{A}_e$ is diagonal, so is the assembled matrix $\mathbf{A}$ and its inverse. These steps permit to evaluate the inverse of the global mass matrix through expression (27) in an efficient way.

Remark 3. The same process can be applied to obtain reciprocal mass matrices for the FEM. The details of the methodology, as well as its application to solid and structural elements, was investigated by the authors[9] in a previous paper.

6.2 | Mass matrix parametrization

A family of reciprocal mass matrices can be constructed by incorporating mass matrix parametrization[38,7,8] into the previous process. Introducing free parameters, we can create a family of inverses and later select the members of this family with best properties for different applications. There exist several ways to parametrize mass matrices at the element level, see Felippa et al.[39] for an exhaustive classification[39], being a consistent-lumped linear combination the simplest choice:

$$\mathbf{M}_e = (1-\beta)\mathbf{M}_e^C + \beta\mathbf{M}_e^L \tag{43}$$

in which a parameter $\beta \in [0, 1]$ is used to balance between the element consistent mass matrix $\mathbf{M}_e^C$ and lumped mass matrix $\mathbf{M}_e^L$. For example, using $\beta = \{0, 1/2, 1\}$ the element mass matrix is then easily reduced respectively to the consistent mass matrix (CMM), averaged mass matrix (AMM) and lumped mass matrix (LMM).

In particular, the case $\beta = 1$ is of no interest because it reduces the reciprocal matrix to the common diagonal LMM with a trivial inverse. LMM computed for IGA by the row-sum technique is very popular in explicit dynamics[15]. Unfortunately, the lumped mass matrix does not maintain the accuracy of the consistent mass matrix for high frequencies and finding better options would suppose an important advantage for explicit dynamics. It is well known that the frequencies by CMM converge from above, whereas the frequencies by LMM converge from below. Then, it remains the task of selecting an appropriated parameter β for B-spline interpolations of different degree with the objective of beating the LMM accuracy with equivalent computational costs. This point will be addressed in the following section.

6.3 | Dispersion analysis

The introduction of a consistent-lumped mass matrix parametrization in the reciprocal mass matrix makes it possible to tune the free parameter β for different objectives, like maximum accuracy for certain frequency ranges. The tool used for evaluating the

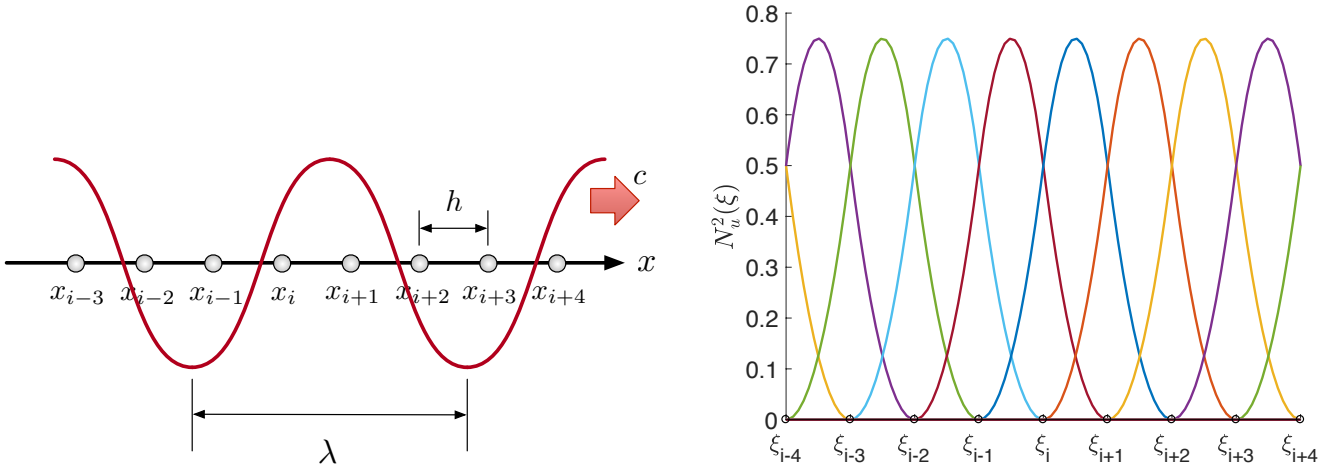

FIGURE 8 A compression wave with velocity c and length λ is assumed to travel in a discretized uniform bar. Infinite one dimensional lattice of equidistant control points (left) and associated quadratic B-spline interpolation functions (right) used for dispersion analysis.

accuracy of a particular reciprocal mass is Fourier analysis[39,40]. For this task, we assume a monochromatic compressive steady wave of frequency ω traveling in a uniform and infinite one-dimensional bar.

The governing equation for longitudinal vibration in an elastic bar has the form:

$$\frac{\partial}{\partial x}\left(EA\frac{\partial u}{\partial x}\right) - \rho A\frac{\partial^2 u}{\partial t^2} = 0 \tag{44}$$

where $u(x,t)$ is the axial displacement, $x \in (-\infty, \infty)$ is the axial coordinate, $t \geq 0$ denotes the time, ρ is the mass density, A is the area of a cross-section and E denotes the Young's modulus. The exact speed of longitudinal waves in an elastic bar[41] is $c_0 = \sqrt{E/\rho}$. Then, we discretize the problem with an uniform infinite mesh of equidistant knots, see Figure 8, to study the effect of IGA discretization and parametrization in the numerically calculated wave speed c for different wave numbers k.

Assuming an interpolation of B-spline functions of order p in an infinite patch, with uniformly distributed knots and characteristic element length h, we can compute analytically the stiffness and mass matrices and later use expression (40) to obtain the elemental momentum matrix. This process starts obtaining the element matrices, for example, for the linear case:

Linear ($p = 1$)

$$\mathbf{K}_e = \frac{EA}{h}\begin{bmatrix} 1 & -1 \\ -1 & 1 \end{bmatrix}, \qquad \mathbf{M}_e^C = \frac{\rho Ah}{6}\begin{bmatrix} 2 & 1 \\ 1 & 2 \end{bmatrix}, \qquad \mathbf{M}_e^L = \frac{\rho Ah}{2}\begin{bmatrix} 1 & 0 \\ 0 & 1 \end{bmatrix} \tag{45}$$

$$\mathbf{A}_e = \frac{Ah}{2}\begin{bmatrix} 1 & 0 \\ 0 & 1 \end{bmatrix}, \quad \mathbf{C}_e = \frac{Ah}{2(1+2\beta)\rho}\begin{bmatrix} (\beta+2) & (\beta-1) \\ (\beta-1) & (\beta+2) \end{bmatrix} \tag{46}$$

and for quadratic B-splines,

Quadratic ($p = 2$)

$$\mathbf{K}_e = \frac{EA}{6h}\begin{bmatrix} 2 & -1 & -1 \\ -1 & 2 & -1 \\ -1 & -1 & 2 \end{bmatrix}, \qquad \mathbf{M}_e^C = \frac{\rho Ah}{120}\begin{bmatrix} 6 & 13 & 1 \\ 13 & 54 & 13 \\ 1 & 13 & 6 \end{bmatrix}, \qquad \mathbf{M}_e^L = \frac{\rho Ah}{6}\begin{bmatrix} 1 & 0 & 0 \\ 0 & 4 & 0 \\ 0 & 0 & 1 \end{bmatrix} \tag{47}$$

$$\mathbf{C}_e = \frac{Ah}{12(1+3\beta)(1+39\beta)\rho}\begin{bmatrix} 39\beta^2+250\beta+31 & 52(3\beta+1)(\beta-1) & (39\beta-23)(\beta-1) \\ 52(3\beta+1)(\beta-1) & 16(3\beta+1)(13\beta+7) & 52(3\beta+1)(\beta-1) \\ (39\beta-23)(\beta-1) & 52(3\beta+1)(\beta-1) & 39\beta^2+250\beta+31 \end{bmatrix} \tag{48}$$

with the momentum matrix expressed as a function of the weighting parameter β, used to interpolate between CMM and LMM.

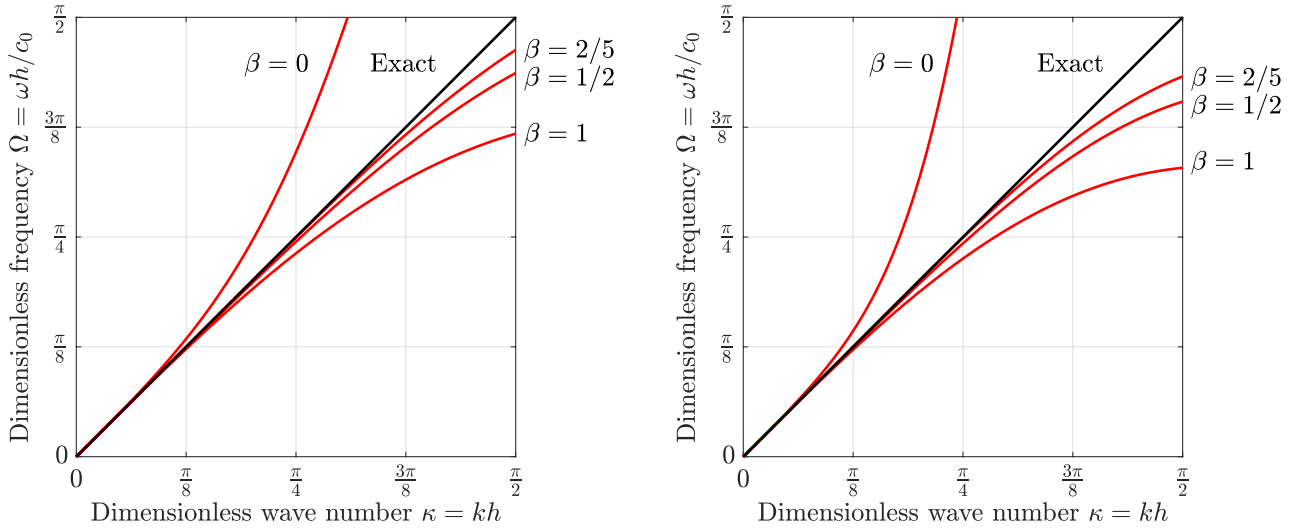

FIGURE 9 Analytical dispersion diagrams for an infinite bar modeled with quadratic p=2 B-splines (left) and cubic p=3 B-splines (right) using different mass scaling parameters. Note that $\kappa = \frac{\pi}{2}$ corresponds to a resolution of four elements per wave length. Divergence is observed for $\beta = 0$ and a minimum dispersion error is obtained for $\beta = 2/5$.

These element matrices are then used to assemble the discrete equations of motion, obtained from momentum (20) and equilibrium (19) equations, particularized for the infinite lattice in the form:

$$\left.\begin{aligned} \mathbf{A}\dot{\mathbf{p}} + \mathbf{K}\mathbf{u} &= \mathbf{0} \\ \mathbf{A}^{\mathsf{T}}\dot{\mathbf{u}} - \mathbf{C}\mathbf{p} &= \mathbf{0} \end{aligned}\right\} \quad \rightarrow \left(\mathbf{A}^{-\mathsf{T}}\mathbf{C}\mathbf{A}^{-1}\mathbf{K}\right)\mathbf{u} - \ddot{\mathbf{u}} = \mathbf{0} \tag{49}$$

from where we have eliminated the momentum variable to finally write the dynamic equilibrium only in terms of displacements.

Next, we force a harmonic solution for the axial displacement in the form:

$$u(x,t) = U e^{i(kx-\omega t)} = U e^{i(\kappa\xi - \Omega c_0 t)/h} \tag{50}$$

with the dimensionless wavenumber κ and frequency Ω respectively defined as $\kappa = kh$ and $\Omega = \omega h/c_0$. Then, we particularize it at the control point coordinates $x_i = \{\dots, -2h, -h, 0, h, 2h, \dots\}$ and substitute back in the equilibrium equation (49) to obtain:

$$\left[\mathbf{A}^{-\mathsf{T}}\mathbf{C}\mathbf{A}^{-1}\mathbf{K} - \left(\frac{\Omega c_0}{h}\right)^2 \mathbf{I}\right]\mathbf{u}^h = \mathbf{0} \tag{51}$$

with a discrete solution vector for displacements:

$$\mathbf{u}^h = U\left[\dots e^{-2i\kappa} e^{-i\kappa}\ 1\ e^{i\kappa} e^{2i\kappa}\ \dots\right]^{\mathsf{T}} \tag{52}$$

obtaining a discrete system that repeats the same equilibrium equation at each location x_i of the lattice.

Finally, the extraction of i^{th} row of system (51) provides us with the sought dispersion equation, relating the dimensionless numerical frequency Ω with the wave number κ and parameter β. This relation is represented in Figure 9 for quadratic (left) and cubic (right) B-spline interpolations and compared with the exact solution for an infinite elastic bar. We observe a divergent result for $\beta = 0$ (CMM) which invalidates the use of that particular RMM for practical purposes. However, it is also observed that convergence is recovered for some positive values of the mass averaging parameter ($\beta > 0$). In particular, a good low-mid frequency fitting is obtained for $\beta = 1/2$, clearly outperforming the accuracy of the LMM ($\beta = 1$).

In order to investigate this divergence issue, we perform a Taylor series expansion of (51) around $\kappa = 0$. For $p = 1$, traditional C^0 linear finite element shape functions, Fourier analysis using element matrices (45) and (46) yields the dispersion relation:

$$\Omega^2 = \kappa^2 + \frac{5 - 8\beta}{12(1 + 2\beta)}\kappa^4 + \mathcal{O}(\kappa^6) \tag{53}$$

revealing that, for lower frequencies, the RMM obtained with mass parametrization diverges for $\beta \in [0, 5/8)$. In particular, it is fourth order accurate for $\beta = 5/8$ and produce acceptable results for $\beta \in [5/8, 1]$.

Similarly, for quadratic B-splines, with element matrices given by (47) and (48), the Taylor expansion with respect to wavenumber κ yields the dispersion relation,

$$\Omega^2 = \kappa^2 + \frac{3-7\beta}{4(1+3\beta)}\kappa^4 + \mathcal{O}(\kappa^6) \tag{54}$$

where it is observed that fourth order approximation can be achieved by using $\beta = 3/7$ and the admissible interval of the averaging parameter is extended to $\beta \in [3/7, 1]$. Moreover, an optimization of parameter β for higher frequencies, see Figure 9 , reveals that the best approximation is obtained for $\beta = 2/5$. Using $\beta = 2/5$ is a compromise to improve accuracy for the higher frequencies, maintaining second order approximation for the lower frequencies. This value has been obtained empirically, minimizing by numerical experiment the dispersion error at $\kappa = \pi/2$.

Remark 4. For B-splines, the RMM obtained with an element-wise LD dual-basis is very cheap to compute but should be used with care. It diverges for $\beta = 0$ (CMM) and is not able to provide accurate results. However, the use of mass parametrization with $\beta \in [2/5, 1)$ always provides a better approximation than the LMM diagonal mass inverse, although p-convergence property is not preserved.

It is worth to mention that this type of LD B-spline dual basis has also been studied mathematically in the context of IGA mortar methods for contact problems by Steiz et al.[31], observing that LD bases generated element-wise only guarantee partition of unity and consequently the *global* approximation order is limited to one in the L^2-norm, independently of the *local* approximation order. This defect in the approximation order of the B-spline dual basis causes that optimal convergence rates cannot be guaranteed. Obviously, our element-wise dual basis reproduce the same convergence problems when utilized for inverse mass matrix computations, but these difficulties can be palliated with mass matrix parametrization techniques[21]. Finally, it has been also investigated the use of sixth-order accurate element mass matrices[42,43,44] instead of the fourth order approximation given by (43) for $\beta = 0$. By adopting these high-order mass matrices, it is possible to increase the accuracy of the RMM, but the improvement is still not enough for its practical use with LD dual bases.

Remark 5. Because the reciprocal mass matrix $\mathbf{C}$ is by definition positive definite, the unsymmetric eigenvalue problem $\left[\mathbf{A}^{-\mathsf{T}}\mathbf{C}\mathbf{A}^{-1}\mathbf{K} - \omega_i^2\mathbf{I}\right]\boldsymbol{\phi}_i = 0$ represented by equation (51) can be converted into a symmetric eigenvalue problem by a Cholesky decomposition of the reciprocal mass matrix with $\mathbf{C} = \mathbf{L}\mathbf{L}^{\mathsf{T}}$, where $\mathbf{L}$ is a lower triangular matrix. Then, the equivalent symmetric eigenvalue problem is obtained:

$$\left[\mathbf{L}^{\mathsf{T}}\mathbf{A}^{-1}\mathbf{K}\mathbf{A}^{-\mathsf{T}}\mathbf{L} - \omega_i^2\mathbf{I}\right]\boldsymbol{\varphi}_i = 0 \tag{55}$$

which has different eigenvectors but the same eigenvalues as the original unsymmetric problem.

7 | INCORPORATION OF BOUNDARY CONDITIONS WITH LAGRANGE MULTIPLIERS

As we mentioned earlier, in the connection with other patches or presence of Dirichlet boundary conditions a direct computation of the mass-inverse requires complicated modifications of the bi-orthogonal shape functions. We eliminate the necessity of these modifications by considering the patches as free-floating substructures and applying the boundary conditions through localized Lagrangian multipliers[10,11,12,13]. To explain the enforcement of boundary conditions, we reorganize the semi-discrete equations of motion (20)-(22) to obtain the following partitioned equation set:

$$\begin{bmatrix} \mathbf{M} & \mathbf{B} & \mathbf{0} \\ \mathbf{B}^{\mathsf{T}} & \mathbf{0} & -\mathbf{L}_b \\ \mathbf{0} & -\mathbf{L}_b^{\mathsf{T}} & \mathbf{0} \end{bmatrix} \begin{Bmatrix} \ddot{\mathbf{u}} \\ \lambda \\ \ddot{\mathbf{u}}_b \end{Bmatrix} = \begin{Bmatrix} \mathbf{r} \\ \mathbf{0} \\ \mathbf{0} \end{Bmatrix} \tag{56}$$

where the second equation is simply twice time-differentiated expression of (21).

Let's assume now that the boundary acceleration vector ($\ddot{\mathbf{u}}_b$) consists of entirely the prescribed boundary quantities, regardless whether they are zero or nonzero. In this case, we obtain the accelerations ($\ddot{\mathbf{u}}$) from the first equation of (56) as:

$$\ddot{\mathbf{u}} = \mathbf{M}^{-1}\left(\mathbf{r} - \mathbf{B}\lambda\right) \tag{57}$$

in which once again we emphasize that the computation of $\mathbf{M}^{-1} = \mathbf{A}^{-\mathsf{T}}\mathbf{C}\mathbf{A}^{-1}$ does not requiere additional computational effort because the global projection matrix $\mathbf{A}$ is diagonal.

Then, substitute the accelerations obtained above into the second equation of (56):

$$\mathbf{B}^{\top}\mathbf{M}^{-1}\left(\mathbf{r}-\mathbf{B}\lambda\right)-\mathbf{L}_b\ddot{\mathbf{u}}_b=\mathbf{0} \tag{58}$$

to compute the Lagrange multipliers:

$$\lambda=\left[\mathbf{B}^{\top}\mathbf{M}^{-1}\mathbf{B}\right]^{-1}\left(\mathbf{B}^{\top}\mathbf{M}^{-1}\mathbf{r}-\mathbf{L}_b\ddot{\mathbf{u}}_b\right) \tag{59}$$

as a function of the forces residual and the boundary conditions. Finally, substitute the multipliers back in the equilibrium equation (57) to obtain the final accelerations:

$$\ddot{\mathbf{u}}=\mathbf{M}_b^{-1}\mathbf{r}+\mathbf{M}^{-1}\mathbf{B}\left[\mathbf{B}^{T}\mathbf{M}^{-1}\mathbf{B}\right]^{-1}\mathbf{L}_b\ddot{\mathbf{u}}_b \tag{60}$$

with a constrained inverse mass matrix:

$$\mathbf{M}_b^{-1}=\mathbf{M}^{-1}-\mathbf{M}^{-1}\mathbf{B}\left[\mathbf{B}^{\top}\mathbf{M}^{-1}\mathbf{B}\right]^{-1}\mathbf{B}^{\top}\mathbf{M}^{-1} \tag{61}$$

incorporating the applied boundary conditions. This transformation can also be understood as a projection of the free-floating mass matrix inverse[9].

Once again, since the size of $\left[\mathbf{B}^{T}\mathbf{M}^{-1}\mathbf{B}\right]$ is small, pertaining only to the constrained degrees of freedom, its inversion is very cheap. It is also noted that $\ddot{\mathbf{u}}$ contains not only the interior but also the constrained degrees of freedom, and the imposition of boundary conditions will produce zeros in the associated rows and columns of $\mathbf{M}_b^{-1}$ making it singular. These zero rows and columns, corresponding to restricted degrees of freedom, can be simply eliminated.

Algorithm 1 Procedure for the computation of the constrained inverse mass matrix $\mathbf{M}_b^{-1}$

for e **do** 1...N_e (elements)
Compute parametrized element mass matrix:
$\mathbf{M}_e=(1-\beta)\mathbf{M}_e^{C}+\beta\mathbf{M}_e^{L}$
Assemble diagonal projection matrix:
$\mathbf{A}_e=\frac{1}{\rho}\mathbf{M}_e^{L}\quad\rightarrow\quad\mathbf{A}=\mathop{\mathsf{A}}_{e=1}^{N_e}\mathbf{A}_e$
Assemble reciprocal mass matrix:
$\mathbf{C}_e=\mathbf{A}_e^{\top}\mathbf{M}_e^{-1}\mathbf{A}_e\quad\rightarrow\quad\mathbf{C}=\mathop{\mathsf{A}}_{e=1}^{N_e}\mathbf{C}_e$
end for
Compute the free-floating inverse mass matrix:
$\mathbf{M}^{-1}=\mathbf{A}^{-\top}\mathbf{C}\mathbf{A}^{-1}$
Obtain the projector:
$\boldsymbol{\mathcal{P}}=\mathbf{I}-\mathbf{M}^{-1}\mathbf{B}\left[\mathbf{B}^{\top}\mathbf{M}^{-1}\mathbf{B}\right]^{-1}\mathbf{B}^{\top}$
Apply boundary conditions by projection:
$\mathbf{M}_b^{-1}=\boldsymbol{\mathcal{P}}\mathbf{M}^{-1}$
Eliminate the rows and columns of $\mathbf{M}_b^{-1}$ with applied boundary conditions

8 | NUMERICAL TESTS

In the following examples, for vibration analyses we seek for an harmonic solutions that satisfy the EOM and fulfill the boundary conditions $\mathbf{u}_b=\mathbf{0}$. These solutions are obtained by solving the following eigenvalue problem:

$$\left[\mathbf{M}_b^{-1}\mathbf{K}_b-\omega^2\mathbf{I}\right]\boldsymbol{\phi}=\mathbf{0} \tag{62}$$

where $\mathbf{M}_b^{-1}$ is the inverse mass matrix computed as described in Section 7 and $\mathbf{K}_b$ is the stiffness matrix incorporating the applied boundary conditions. From the solution of this eigenvalue problem, we obtain the vibration frequencies ω_i of the system and its associated mode shapes $\boldsymbol{\phi}_i$ for mode number $i=1,\dots n$.

In time-domain analyses, for time integration of the semi-discrete equations of elastodynamics, we use the classical explicit central difference scheme[45,46,47]. This method is among the most popular explicit methods in computational mechanics[4], based on a repetition of the basic steps summarized in Algorithm 2 until the total simulation-time has been reached.

Algorithm 2 Explicit time integration by central difference scheme

Solve time $t = 0$:
$\ddot{\mathbf{u}}^0 = \mathbf{M}_b^{-1}\mathbf{r}^0$
for n **do** 1...n (time steps)
  Evaluate the forces residual:
  $\mathbf{r}^n = \mathbf{f}^n - \mathbf{K}_b\mathbf{u}^n$
  Compute accelerations:
  $\ddot{\mathbf{u}}^n = \mathbf{M}_b^{-1}\mathbf{r}^n$
  Update nodal velocities:
  $\dot{\mathbf{u}}^{n+\frac{1}{2}} = \dot{\mathbf{u}}^{n-\frac{1}{2}} + \Delta t\ddot{\mathbf{u}}^n$
  Update nodal displacements:
  $\mathbf{u}^{n+1} = \mathbf{u}^n + \Delta t\dot{\mathbf{u}}^{n+\frac{1}{2}}$
end for

It is well known that the explicit central difference scheme in linear dynamics is conditionally stable, so the time-step Δt must be chosen below a critical value $\Delta t_{crit} = 2/\omega_{max}$, where ω_{max} is the maximum frequency of the system. We have seen that the proposed RMM with parametrization, obtained following the process described in Section 4, is able to retain accuracy the for lower frequencies reducing highest frequencies at the same time. This reduction automatically increases the critical time-step, allowing the use of larger time steps and improving the computational efficiency.

To evaluate all element matrices we have used a Gauss-Legendre quadrature formula[1] of degree $p+1$ over the knot intervals, where p is the order of the used B-spline or Bézier interpolation function. For the presentation of results we have adopted the following nomenclature. Plots with labels IGA and IGA-BE are used as a reference, indicating results obtained with the exact IGA mass matrix inverse, computed respectively with B-splines or Bézier extraction. The proposed reciprocal matrix is referred as RMM and RMM-BE depending on the interpolation functions, B-splines or Bézier elements, respectively.

8.1 | Free vibration of a bar

In this first example, we analyze the accuracy of the proposed method for direct computation or reciprocal mass matrices by analyzing the free vibration of elastic bars. For this purpose we consider we consider a long bar of length $L = 1$ m of uniform section. The material of the bar is linear elastic, with Young's modulus $E = 69$ GPa and constant volumetric mass density $\rho = 2700\,\mathrm{kg/m^3}$.

The bar is discretized using a linear parameterization of 43 control points to investigate the accuracy of the RMM for quadratic and cubic $p = 2, 3$ orders of longitudinal displacement discretization. In particular, we investigate differences in the use of exact IGA inverses of the CMM and LMM matrices and the proposed approximation of the mass matrix inverse RMM computed with an optimized β.

8.1.1 | Free-free case

We start with the free-free case, by comparing the numerical frequencies with exact solutions obtained from continuum theory. The exact frequencies of this problem are $\omega_n^{exact} = (n-1)c_0\pi/L$ rad/s for mode number $n = 1, 2, \ldots$ where $c_0 = \sqrt{E/\rho}$ is the wave speed of compressive waves and $n = 0$ provides a zero eigenfrequency corresponding to the free rigid body motion.

Results for this case are presented in Figure 10 for two orders of approximation, quadratic $p = 2$ on the left and cubic $p = 3$ on the right, and two different discretization methods, B-splines on the top and Bézier extraction at the bottom. We include frequencies for the exact inverse of the IGA mass matrix, for CMM $\beta = 0$, optimized $\beta = 2/5$ and LLM $\beta = 1$ cases. For comparison, the RMM computed with the proposed method and optimized parameter $\beta = 2/5$ is also included.

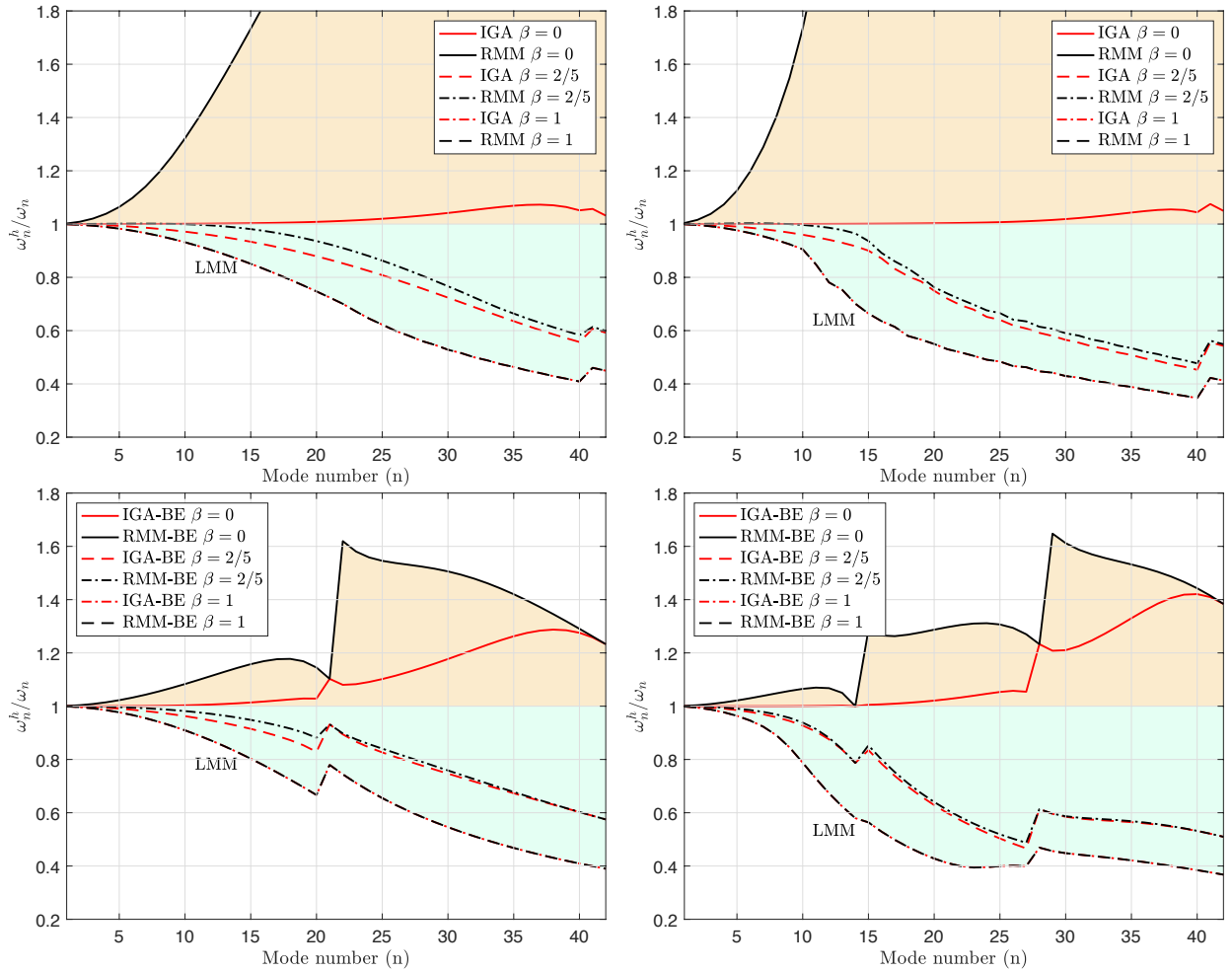

FIGURE 10 Free-free bar vibration problem computed with LD dual basis. Error in the frequencies for quadratic $p = 2$ (left) and cubic $p = 3$ (right) orders using B-splines (top) and Bézier extraction discretizations (bottom). The RMM with $\beta = 0$ (CMM) produces divergent results for B-splines and p-convergent behaviour for Bézier elements. In all cases, RMM with an optimized parameter $\beta = 2/5$ are able to capture correctly the low frequency band providing higher accuracy than LMM ($\beta = 1$) for the full frequency spectrum.

It is well known[27,48] and evident from inspection of Figure 10 (top) that, by increasing the order p of the LMM inverse, higher-order accuracy is not achieved. We also observe that the present method, using the RMM with $\beta = 2/5$, yields far better accuracy than the LMM for all frequencies. With quadratic B-splines, the optimized RMM is able to approximate almost half of the spectrum with good accuracy, first 20 modes are below 5% error while for cubic order it is reduced to the 15 first modes approximately. But in general, increasing the approximation order either for B-spline or Bézier approximations, expands the nonzero elements of the banded mass matrix and reduces the accuracy in the mid and high frequency range.

The RMM for Bézier elements, on the contrary, is completely stable for $\beta = 0$ conserving the p-convergence property, see Figure 10 (bottom) for cases p=2,3. It can also be observed that although Bézier extraction introduces higher branching in the spectrum[49], its accuracy is very close to the B-splines approximation. This branching is caused by the two distinct types of equations for the Bézier based elements: those corresponding to nodes located at the element boundaries, and those corresponding to the internal nodes located inside the element[27]. Note that the number of branches coincide with the Bézier element degree.

Moreover, RMM produces a maximum frequency around 40% lower than the exact IGA consistent matrix (IGA $\beta = 0$), so the critical time-step for explicit time integration with the RMM can be reduced by the same amount. This is close to the 55% reduction of the diagonal LMM but without so much degradation of the accuracy for the low frequencies.

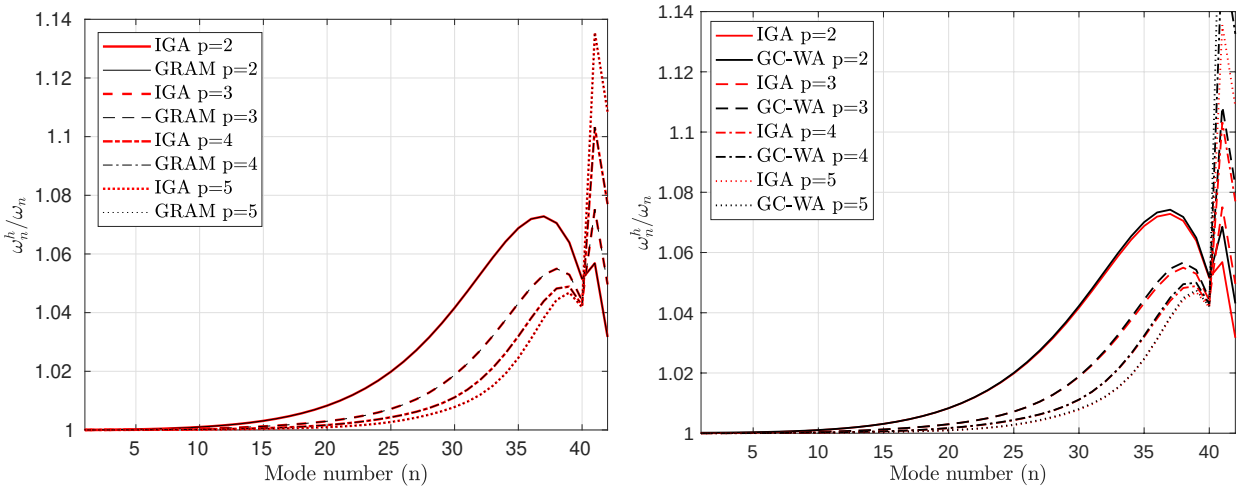

FIGURE 11 Error in the natural frequencies of a free-free bar computed using GC dual bases. The inverse *Gram* matrix (left) and the *weight-adjusted* (GC-WA) basis (right) produce p-convergent approximations. These GC bases provide high accuracy, but at the price of elevated computational cost in the case of the *Gram* matrix and loss of generality for the *weight-adjusted* basis.

Finally, we explore the accuracy of GC dual bases in the bar frequencies. In particular we use the inverse *Gram* matrix and the *weight-adjusted* to compute the RMM for different B-spline basis orders. The results are shown in Figure 11, where it is observed that the frequency error is totally equivalent to the IGA mass matrix and p-converge is maintained. Once again, note that the evaluation of these two reciprocal bases require two costly operations, invert the Gramian matrix (left) and invert the mass matrix of the parametric domain (right), but nevertheless these operations are cheaper than the inversion of the original mass matrix.

8.1.2 | Fixed-free bar

Now, to test the proposed technique for applying boundary conditions using localized Lagrange multipliers described in Section 7, we proceed to fix the displacement of the first control point located on the left side of the bar. In terms of frequencies, the only difference with the free-free case is in the restriction of the rigid body motion of the bar and the shift of exact frequencies to $\omega_n^{exact} = (n-1/2)c_0\pi/L$ for mode number $n = 1, 2, \ldots$.

Figure 12 contains the results obtained for this case. We corroborate that accuracy is not affected by the imposition of boundary conditions through localized Lagrange multipliers and the results are completely equivalent. In this case we have tested the RMM with $\beta = 2/5$ that provides very similar approximation of the bar frequencies. The results confirm that using the present method to approximate the inverse mass matrix yields much better accuracy than the LMM with similar computational effort.

8.2 | Free vibration of a cantilevered tapered plate - FV32 test

This example is a plane-stress test proposed by the National Agency for Finite Element Methods and Standards[50]. In particular the dynamic case FV32 for checking the accuracy of flexural and longitudinal modes, where the natural frequencies of a trapezoidal elastic plate are analyzed. The geometry and dimensions of the plate are represented in Figure 13 together with the boundary conditions. It is assumed a linear elastic material with Young's modulus $E = 200$ GPa, Poisson's ratio $\nu = 0.3$, and density $\rho = 8000\ \mathrm{kg/m^3}$.

First, the plate is discretized using a single patch with a regular mesh of 10×10 control points and quadratic isogeometric NURBS-based elements, constraining the horizontal and vertical displacements of the 10 control points located at $x = 0$, a lateral side of the plate. The knot points vector $\Xi = \{0, 0, 0, 0.125, 0.25, 0.375, 0.5, 0.625, 0.75, 0.875, 1, 1, 1\}$ is used in each direction to construct a regular 2D patch $\Xi \times \Xi$ with B-splines of order $p = 2$.

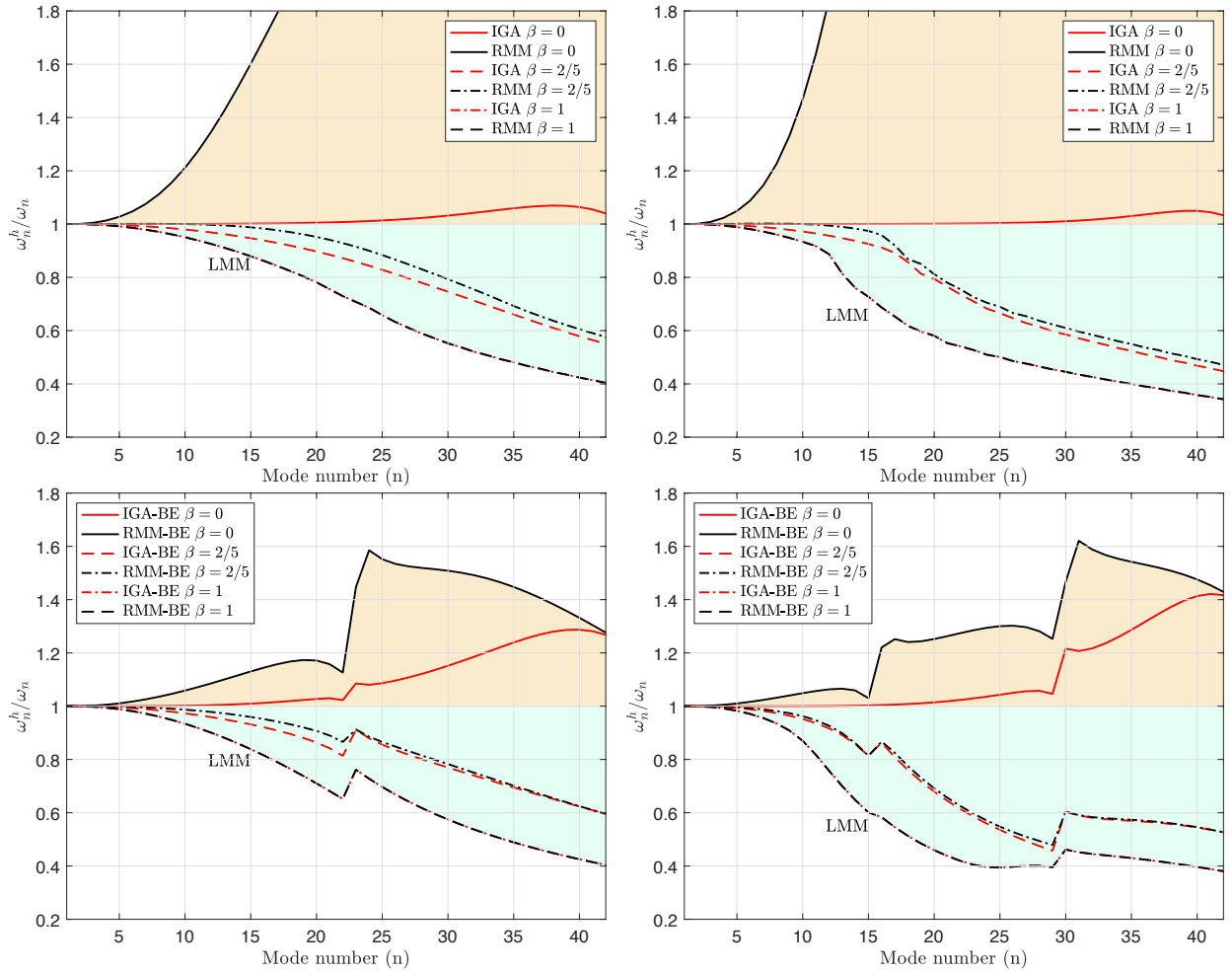

FIGURE 12 Fixed-free bar problem computed with LD dual basis. Error in the frequencies for quadratic $p = 2$ (left) and cubic $p = 3$ (right) orders using B-splines (top) and Bézier extraction discretizations (bottom). We observe that RMM with $\beta = 0$ (CMM) produces divergent results for B-splines and p-convergent behaviour for Bézier elements. In all cases, RMM with an optimized parameter $\beta = 2/5$ are able to capture correctly the low frequency band providing higher accuracy than LMM ($\beta = 1$) for the full frequency spectrum..

Next, the Bézier extraction process is applied to the patch of quadratic B-splines, see Figure 14 , producing a mesh of 5×5 Bézier elements with 11×11 nodes. Note that in both cases, these are more refined meshes than the one proposed in the original NAFEMS benchmark case, that uses quadrilateral finite elements.

This is a particular example where the *weight-adjusted* dual basis (34) is readily applicable, because the parametric domain is completely regular and the parametrical-to-physical geometrical transformation is an affine mapping, hence Jacobian of the transformation is constant.

The first 9 mode shapes of the plate are illustrated in Figure 15 and their associated frequencies, obtained with different mass matrix inverses, arranged in Table 1 . As a reference, we use the frequencies computed with the original mass matrix, IGA or IGA-BE (CMM). These frequencies are very close to the NAFEMS test for FEM and results from other authors obtained with different RMM proposals.

First, we note that GC-Gram and GC-WA bases produce exactly the same frequencies and are able to approximate the correct values with negligible error, confirming once again the superiority of these GC bases over the LD ones. Nevertheless, the LD-RMM computed with $\beta = 2/5$ provides a very good fit, with maximum difference obtained respectively in the fourth mode with 1.8% error and the fifth mode with 4.9% error. Note that they correspond to flexural modes that are more difficult to capture

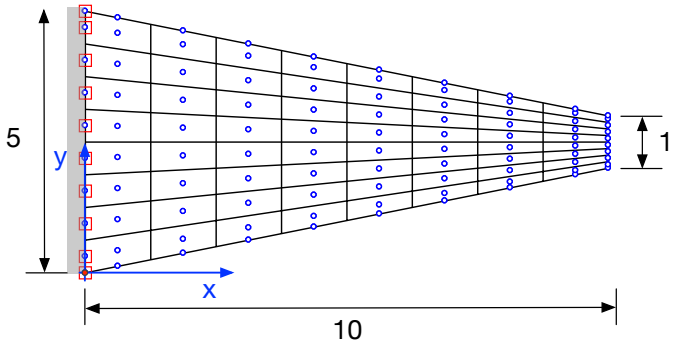

FIGURE 13 NAFEMS benchmark case FV32. Geometry with dimensions in meters and zero boundary displacements imposed on the lateral side of the plate at $x = 0$. The IGA regular mesh presents $l \times m = 10 \times 10$ control points, indicated in blue and uses quadratic B-spline interpolation functions in both directions.

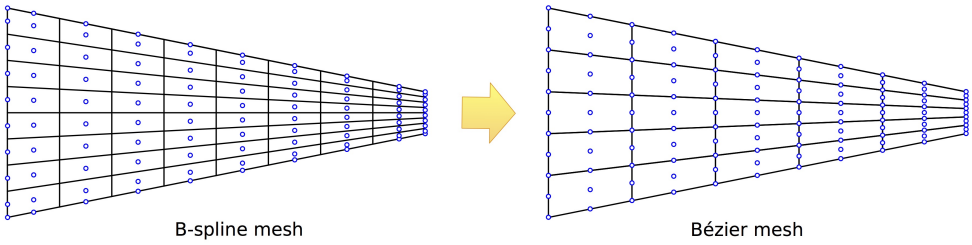

FIGURE 14 A computational IGA mesh based on B-spline shape functions (on the left) and based on Beziér shape functions after Beziér extrapolation (on the right).

than extension modes, see Figure 15. For Bézier elements, maximum errors correspond to the same flexural modes with values under 8%.

In general, it is verified that the proposed RMM obtained with LD bases and mass-matrix parametrization is a better alternative than the LMM for all modes.

8.3 | Free vibration of a clamped thin circular plate

This numerical example is inspired by the paper of Cottrell et al.[22], where the problem of free vibration of a thin circular plate is solved. The purpose of this example is to show the behavior of the proposed method also for a domain with a curved boundary. The circular plate has a radius $r = 2$ m and thickness $t = 0.02$ mm. Although it would seem natural to model the plate using shell finite elements, we follow the paper[22] and model the circular plate as a three-dimensional body. Material of the plate is considered to be linear elastic with Young's modulus $E = 30$ GPa, Poisson's ratio $\nu = 0.2$, and density $\rho = 2320\ \mathrm{kg/m^3}$.

Similar to the preceding example, the plate is first discretized using a single patch with a regular mesh of $18 \times 18 \times 3$ control points and quadratic isogeometric NURBS-based elements, clamping of the control points located at $x^2 + y^2 = r^2$ as represented in Figure 16. The knot vectors $\Xi_1 = \Xi_2 = \{0, 0, 0, 1/16, 2/16, \ldots, 15/16, 1, 1, 1\}$ and $\Xi_3 = \{0, 0, 0, 1, 1, 1\}$ are used in each parametric direction to construct a 3D patch $\Xi_1 \times \Xi_2 \times \Xi_3$ with NURBS of order $p = 2$. Details regarding the used parameterization can be found in the work[51].

Again, the Bézier extraction process is applied to the patch of quadratic B-splines, see Figure 17, producing a mesh of $8 \times 8 \times 1$ Bézier elements with $17 \times 17 \times 3$ control points.

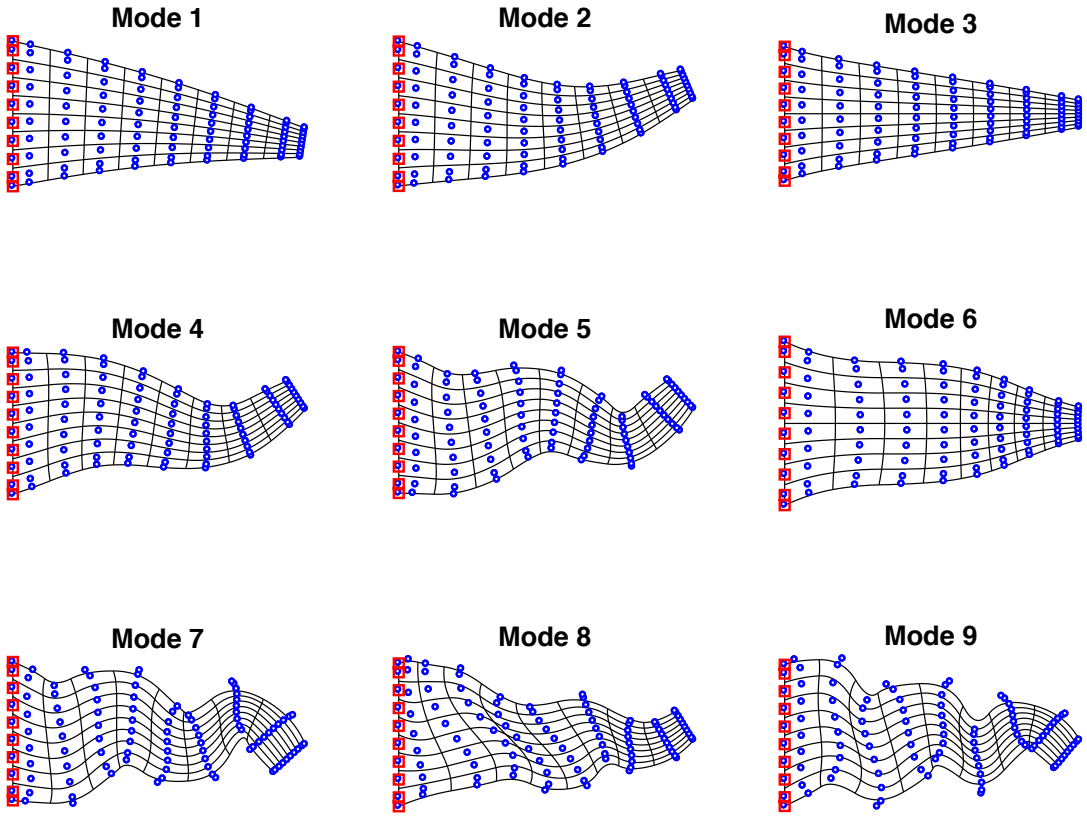

FIGURE 15 NAFEMS benchmark case FV32. Representation of the 9 lowest vibration modes occurring at frequencies contained in Table 1. Results correspond to the proposed reciprocal mass matrix with parameter $\beta = 2/5$ computed with quadratic B-splines.

The three first symmetric ω_{01}, ω_{11} and antisymmetric ω_{02} eigenmodes[22] are illustrated in Figure 18, and their associated frequencies, obtained with different mass matrix inverses, summarized in Table 2. Classical IGA with CMM gives the first three eigenmodes at frequencies $\omega_{01} = 57.636$ rad/s, $\omega_{11} = 127.061$ rad/s, and $\omega_{02} = 260.913$ rad/s that are used as a reference. Note that GC-Gram basis produces again a perfect approximation. As predicted by dispersion analysis, the LD-RMM with best fit is obtained for $\beta = 2/5$, see IGA RMM results in Table 2, presenting discrepancies of 0.05%, 0.04% and 0.2% respectively.

Observing now the IGE-BE (CMM) solution, a slightly poorer approximation is obtained for the Bézier extraction results, compared to IGA with NURBS basis functions. The average relative errors for the Bézier extraction for eigenfrequencies ω_{01}, ω_{11}, and ω_{02} are 0.3%, 0.8% and 2%, respectively. It is important to mention again that the accuracy of the results for LC-RMM crucially depends on the selection of an appropriated value for the parametrization factor β. Its value has been derived from one dimensional dispersion analyses and its optimization for 2D cases deserves further study.

8.4 | Transient analysis of a cantilever beam under self weight

Finally, to test the RMM with a transient case, we consider a 3D cantilever beam under self weight with a sudden application of the gravity load at time $t = 0$ s. The geometrical definition of the problem is shown in Figure 19 (left), where a cantilever beam of length $L = 10$ m and section width $b = 4$ m with height $h = 2$ m is considered. The elastic material properties of the beam are $E = 10$ MPa, $\nu = 0.3$ and density $\rho = 100\,\mathrm{kg/m^3}$ with a gravity acceleration $g = 9.81\,\mathrm{m/s^2}$.

The parametric domain is defined by a 3D patch constructed with knot spans on each direction $\Xi_1 = \{\xi_1, \dots, \xi_{l+p+1}\}$ with $\Delta\xi = 1/19$, $\Xi_2 = \{\eta_1, \dots, \eta_{m+p+1}\}$ with $\Delta\eta = 1/5$ and $\Xi_3 = \{\mu_1, \dots, \mu_{n+p+1}\}$ with $\Delta\mu = 1/3$. Quadratic B-splines with $p = 2$ are used in the three directions. Elements are defined in the parametric space $\Xi_1 \times \Xi_2 \times \Xi_3$ as non-zero knot spans, $[\xi_i, \xi_{i+1}] \times [\eta_i, \eta_{i+1}] \times [\mu_i, \mu_{i+1}]$ and elements in the physical space are images of their parametric counterparts.

TABLE 1 Plane-stress case FV-32 from NAFEMS. Six lowest frequencies obtained with different mass matrices.

Frequency (Hz)	Mode 1	Mode 2	Mode 3	Mode 4	Mode 5	Mode 6
NAFEMS[50] (FEM)	44.623	130.03	162.70	246.05	379.90	391.44
Tkachuk et al.[8] (FEM)	45.499	133.55	162.89	255.37	393.16	398.56
Schaeuble et al.[21] (IGA) VSRMS†	44.615	128.489	162.860	235.104	335.874	385.989
IGA $\beta = 0$ (CMM)	44.634	130.107	162.709	246.639	382.937	391.525
IGA $\beta = 1$ (LMM)	44.022	122.936	161.413	218.492	308.210	373.077
LD-RMM $\beta = 2/5$	44.645	129.581	162.720	241.956	363.728	390.592
GC-Gram	44.634	130.107	162.709	246.639	382.937	391.525
GC-WA	44.634	130.107	162.709	246.641	382.961	391.526
IGA-BE $\beta = 0$ (CMM)	44.651	130.343	162.730	248.396	389.846	391.848
IGA-BE $\beta = 1$ (LMM)	44.096	123.304	161.532	219.363	309.573	374.468
LD-RMM-BE $\beta = 2/5$	44.544	128.531	162.489	238.999	358.320	387.791

The cited references use different meshes and methods.
†Variationally scaled consistent inverse mass matrices.

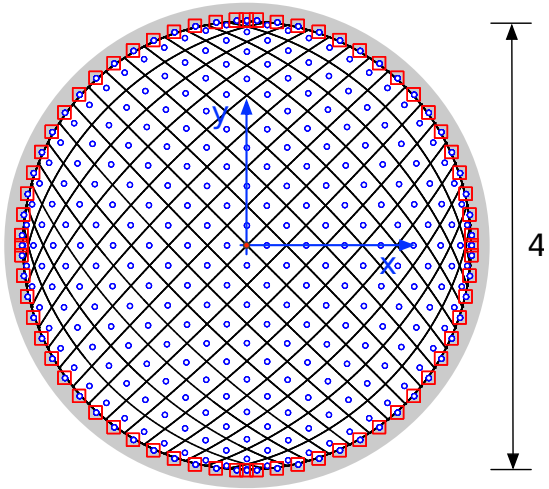

FIGURE 16 Clamped thin circular plate. Geometry with diameter in meters and zero boundary displacements imposed on the lateral side of the plate at $x^2 + y^2 = 4$. The IGA mesh presents $l \times m \times n = 18 \times 18 \times 3$ control points, indicated in blue and uses quadratic NURBS interpolation functions in all three directions.

This patch describes the physical domain with a mesh of $l \times m \times n = 21 \times 7 \times 5 = 735$ control points, producing a total number of $735 \times 3 = 2205$ unknowns except for those control points located at the plane $x = 0$ that are restricted in the three directions of space.

An exact eigenvalue analysis of the problem with a CMM reveals that the maximum frequency of the structure is $\omega_{max} = 3510.5$ rad/s, hence the critical time step for stability of the central difference scheme is $\Delta t_{crit}^{IGA} = 5.7 \times 10^{-4}$ s. This critical time step is utilized to compute the reference solution of the problem. The use of RMM with $\beta = 2/5$ reduces the maximum frequency to $\omega_{max} = 1554.8$ rad/s, increasing the critical time step to $\Delta t_{crit}^{RMM} = 0.0013$ s, i.e., 2.3 times larger than the initial critical time step. Then, a time step $\Delta t = 0.001$ s is selected to perform time-domain analysis, integrating in time the response of the beam with the explicit central difference method described in Algorithm 2. It is observed in Figure 19 (right) that this large time-step $\Delta t \gg \Delta t_{crit}^{IGA}$ produces unstable results with classical IGA, while the RMM with $\Delta t \leq \Delta t_{crit}^{RMM}$ is able to obtain

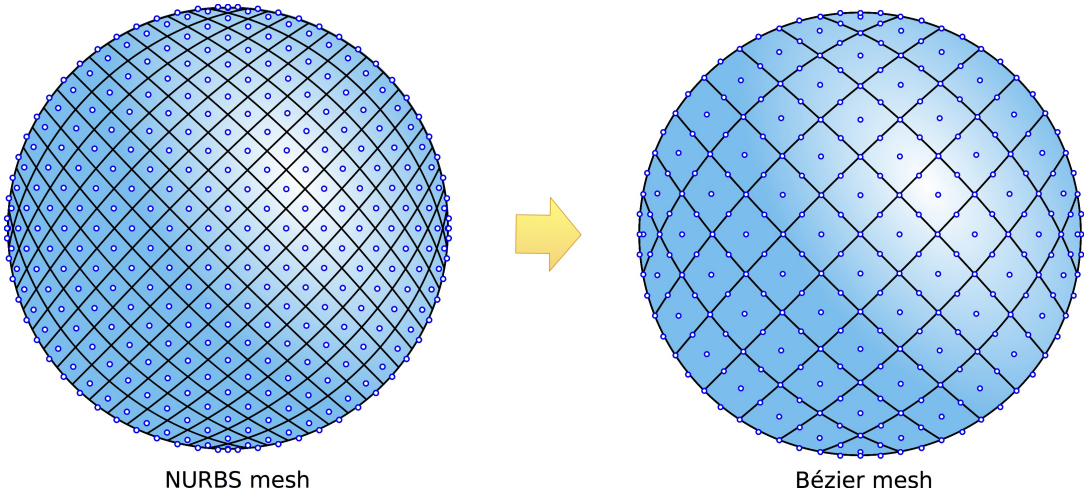

FIGURE 17 A computational IGA mesh based on NURBS basis functions (on the left) and based on Beziér shape functions after Beziér extrapolation (on the right).

TABLE 2 Clamped thin circular plate. Three lowest eigenfrequencies obtained with different mass matrices.

	IGA			Bézier extraction		
Frequency (rad/s)	ω_{01}	ω_{11}	ω_{02}	ω_{01}	ω_{11}	ω_{02}
IGA $\beta = 0$ (CMM)	57.636	127.061	260.913	55.933	119.250	231.591
IGA $\beta = 1$ (LMM)	56.947	123.291	245.604	55.022	114.317	211.815
LD-RMM $\beta = 2/5$	57.666	127.114	260.358	55.774	118.274	226.896
GC-Gram	57.636	127.061	260.914	-	-	-

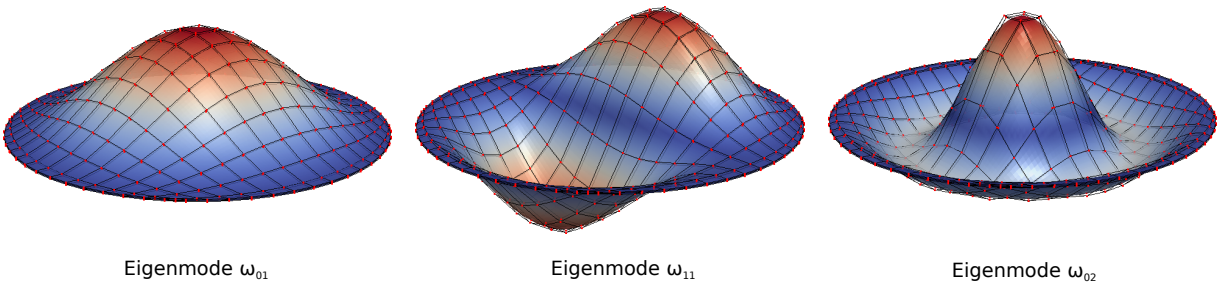

FIGURE 18 Clamped thin circular plate. Two symmetric and one antisymmetric vibration modes corresponding respectively to frequencies ω_{01}, ω_{02} and ω_{11}.

a stable and very accurate solution. In all the cases, initial conditions of the beam are assumed to be zero displacements and velocities, applying the full gravity load at the initial time-step.

The results are shown in Figures 19 and 20 for NURBS and Figure 21 for Bézier elements. We have selected for comparison the RMM computed with different values of the parameter $\beta = \{0, 2/5, 1/2, 1\}$, representing the evolution of the tip deflection of the beam with both approximation methods in Figures 19 (right) and 21 (left). We also compare the time evolution of total internal U, external W and kinetic T energies.

Finally, in Figure 20 (right) it is represented the relative error $(u - u_{exact})/|u_{exact}|$ of the tip displacement u, computed with the proposed RMM ($\beta = 2/5$). It is observed that the error remains under 0.12% during the 1.5 s of simulation, indicating a very good agreement with the reference solution.

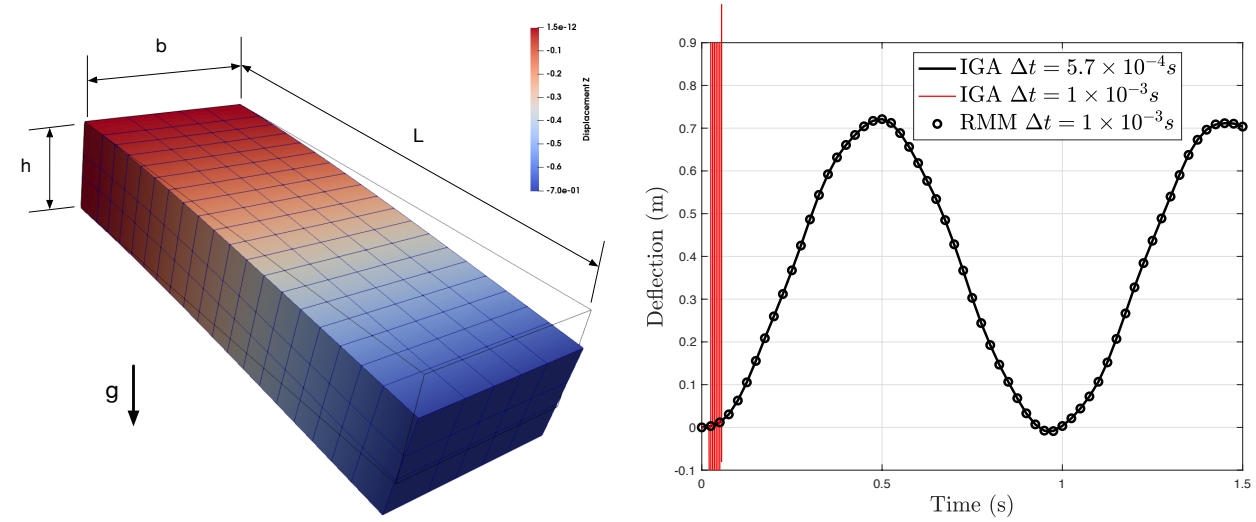

FIGURE 19 Cantilever beam under sudden gravity load. Geometry, dimensions and mesh with elements defined in the physical space. Deformation with contours of vertical displacement at time $t = 1.5$ s computed with the reciprocal mass matrix RMM (left). Comparison of tip deflections $|u_z|$ obtained with explicit IGA and critical time step, IGA with large time-step and the reciprocal mass matrix RMM with $\beta = 2/5$ (right).

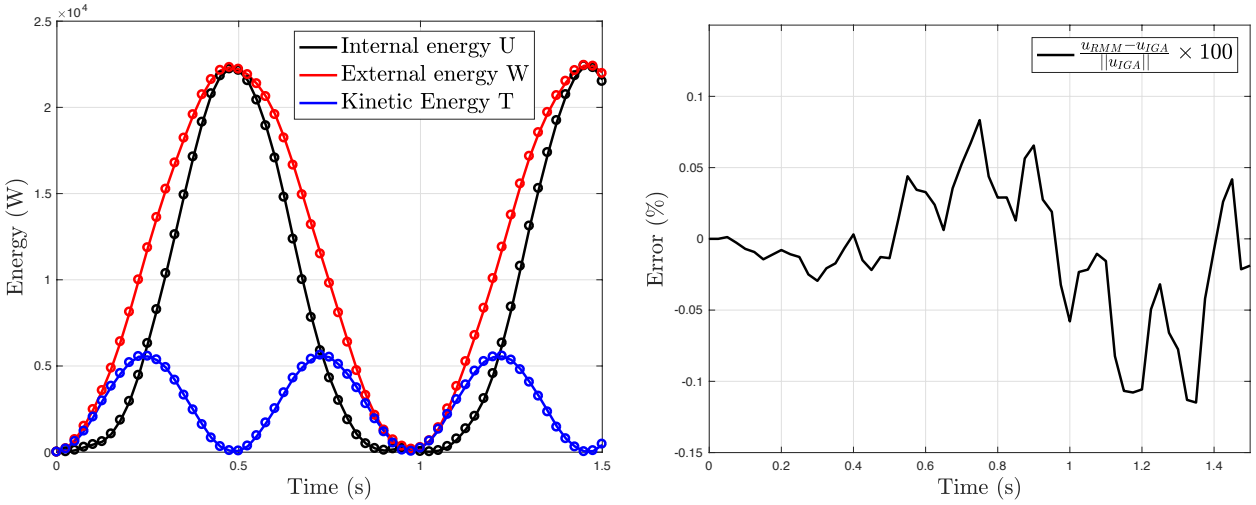

FIGURE 20 Results of the tip loaded cantilever beam. Evolution of the internal, external and kinetic energies in the beam (left). Solutions obtained using the proposed RMM inverse matrix are represented with dots. Error evolution of the beam tip deflection computed with RMM $\beta = 2/5$ (right).

9 | CONCLUSIONS

In structural dynamics, classical explicit time-integration methods equipped with a direct solver require an initial factorization of the mass matrix and repeat subsequent forward and backward substitution operations every time step. If we choose Cholesky factorization, for example, the total cost of this process is around $\mathcal{O}(n^3/3)$ flops plus $\mathcal{O}(2n^2)$ operations per time step for each forward-backward substitution. With a direct approximation of the inverse mass matrix, factorization cost is eliminated and operation count per time step is reduced to a sparse-matrix vector multiplication $\mathcal{O}(mn)$ flops, where m is the average number of nonzero entries per row.

This work presents a variational framework for the direct generation of inverse mass matrices that can be used for the isogeometric analysis of elastodynamic problems. The method requires the definition of an appropriated dual basis for the momentum

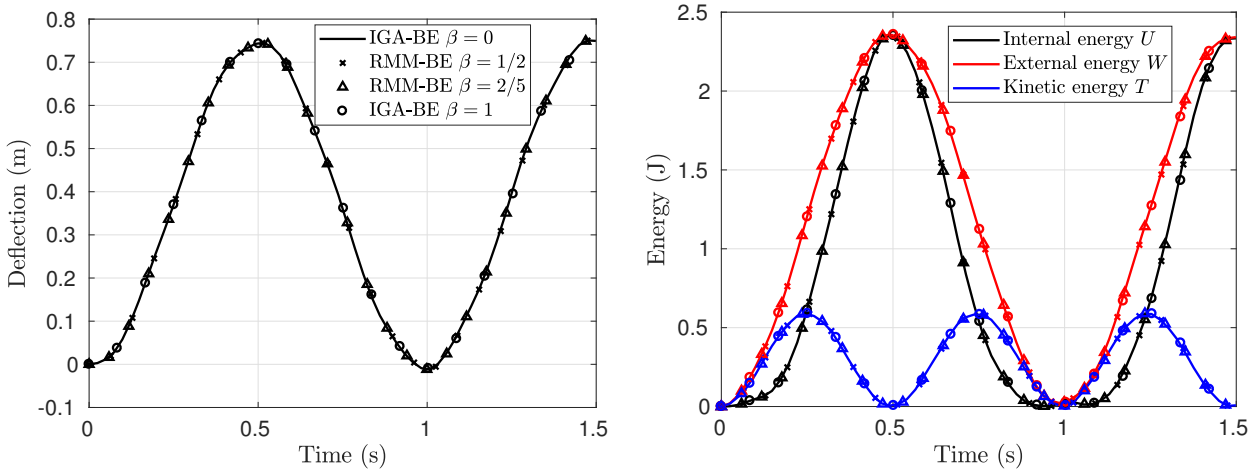

FIGURE 21 Results of the tip loaded cantilever beam discretized by the Bézier elements. Comparison of tip deflections $|u_z|$ obtained with the exact consistent and lumped mass matrices (IGA) and the reciprocal mass matrix (RMM) with parameters $\beta = 1/2$ and $\beta = 2/5$ (left). Evolution of the internal, external and kinetic energies in the beam (right).

field and the influence of the selected reciprocal basis in the efficiency and accuracy of the results has been analyzed for the case of B-splines and Bézier elements. In particular, three types of dual bases have been studied: one local discontinuous (LD) and two global continuous (GC) based respectively on the inverse *Gram* matrix and a *weight-adjustment* of the primal basis through the Jacobian of the transformation.

It is observed that, in terms of computational efficiency and accuracy, LD dual basis combined with mass matrix parametrization produces a RMM that can be a better alternative than the LMM for all frequencies and IGA approximation orders. However, element-wise construction of LD dual basis functions for B-splines with the CMM ($\beta = 0$), produces divergent results. That is not the case for other approximations with C^0 continuity, like Bézier and high order isoparametric finite elements for example, that produce RMMs which retain the p-convergence property for $\beta = 0$. In general, the combination of mass averaging ($\beta > 0$) with LD bases forbids p-convergence for B-spline and Bézier elements of order $p \geq 2$. On the contrary, the GC *Gram* basis is able to achieve high accuracy for any approximation order. Nevertheless, global dual bases produce fully populated inverses and entail higher computational costs. The inverse *Gram* basis requires the inversion of a block-diagonal symmetric matrix and *weight-adjusted* dual basis computational efficiency greatly depends on the regularity of the mesh defined on the parametric space. Moreover, the final inverse mass matrix becomes a fully populated symmetric matrix.

In the present method, inter-patch compatibility and Dirichlet boundary conditions are handled by the method of localized Lagrange multipliers. This process is completely general, avoids the need for dual basis function modifications near the boundary conditions and is found to be computationally efficient because it only requires the factorization of a small element-like matrix associated with the constrained DOFs.

In conclusion, the proposed variational framework for the computation of IGA inverse mass matrices is completely general but, in terms of accuracy and efficiency, its results are influenced by a proper selection of the dual basis. The investigation of analytical LC basis for high-dimensional NURBS and more efficient algorithms for the GC dual basis computation remain an open issue, which we will consider in future work.

ACKNOWLEDGEMENTS

The work of J. Kopačka and R. Kolman was supported by the Centre of Excellence for nonlinear dynamic behaviour of advanced materials in engineering CZ.02.1.01/0.0/0.0/15 003/0000493 (Excellent Research Teams) in the framework of Operational Program Research, Development and Education, and the grant projects of the Czech Science Foundation, No. 17-22615S, No. 17-12925S and No. 16-03823S within institutional support RVO:61388998. S.S. Cho was partially supported by the Nuclear Safety Research Program through the Korea Foundation of Nuclear Safety (KOFONS), granted financial resource from the Nuclear Safety and Security Commission (NSSC), Republic of Korea (No. 1503003).

References

1. Hughes Thomas J R. *The Finite Element Method: Linear Static and Dynamic Finite Element Analysis*. Dover Publication; 2000.

2. Zienkiewicz Olek C, Taylor Robert L, Zhu J Z. *The Finite Element Method: Its Basis and Fundamentals*. Butterworth-Heinemann; 6 ed.2005.

3. Wu Shen R, Wu Lei. *Introduction to the explicit finite element method for nonlinear transient dynamics*. John Wiley & Sons, Inc.; 2012.

4. Belytschko T., Liu W.K., Moran B., Elkhodary K.. *Nonlinear Finite Elements for Continua and Structures*. John Wiley & Sons, Ltd.; 2nd ed.2014.

5. Garoni Carlo, Speleers Hendrik, Ekström Sven-Erik, Reali Alessandro, Serra-Capizzano Stefano, Hughes Thomas J. R.. *ymbol-based analysis of finite element and isogeometric B-spline discretizations of eigenvalue problems: Exposition and review.* ICES REPORT 18-16: The Institute for Computational Engineering and Sciences, The University of Texas at Austin; 2018.

6. Tkachuk A, Wohlmuth B I, Bischoff M. Hybrid-mixed discretization of elasto-dynamic contact problems using consistent singular mass matrices. *International Journal for Numerical Methods in Engineering.* 2013;94(5):473–493.

7. Tkachuk Anton, Bischoff Manfred. Local and global strategies for optimal selective mass scaling. *Computational Mechanics.* 2014;53:1197–1207.

8. Tkachuk Anton, Bischoff Manfred. Direct and sparse construction of consistent inverse mass matrices: general variational formulation and application to selective mass scaling. *International Journal for Numerical Methods in Engineering.* 2015;101(6):435–469.

9. González José A., Kolman R., Cho S. S., Felippa C. A., Park K. C.. Inverse Mass Matrix via the Method of Localized Lagrange Multipliers. *International Journal for Numerical Methods in Engineering.* 2017;113(2):277–295.

10. Park K. C., Felippa C. A.. A variational framework for solution method developments in structural mechanics. *Journal of Applied Mechanics.* 1998;65(1):242–249.

11. Park K. C., Felippa C. A.. A variational principle for the formulation of partitioned structural systems. *International Journal for Numerical Methods in Engineering.* 2000;47:395–418.

12. Park K. C., Felippa C. A., Gumaste U. A.. A localized Version of the method of Lagrange multipliers and its applications. *Computational Mechanics.* 2000;24(6):476–490.

13. González José A, Park K C, Felippa Carlos, Abascal Ramón. A formulation based on localized Lagrange multipliers for BEM-FEM coupling in contact problems. *Computational Methods in Applied Mechanics and Engineering.* 2008;197:623–640.

14. Auricchio F, Veiga L Beir Hughes T J R, Reali A, Sangalli G. Isogeometric collocation methods. *Mathematical Models and Methods in Applied Sciences.* 2010;20(11):2075–2107.

15. Auricchio F, Beirão da Veiga L, Hughes T J R, Reali A, Sangalli G. Isogeometric collocation for elastostatics and explicit dynamics. *Computational Methods in Applied Mechanics and Engineering.* 2012;249–252:2–14.

16. Gao Longfei, Calo Victor M.. Fast isogeometric solvers for explicit dynamics. *Computer Methods in Applied Mechanics and Engineering.* 2014;274:19–41.

17. Sangalli G., Tani M.. Isogeometric preconditioners based on fast solvers for the Sylvester equation. *SIAM Journal on Scientific Computing.* 2016;6(38):A3644–A3671.

18. Hofreither C., Takacs S.. Robust multigrid for isogeometric analysis based on stable splittings of spline spaces. *SIAM Journal on Numerical Analysis.* 2017;55:2004–2024.

19. Donatelli M., Garoni C., Manni C., Serra-Capizzano S., Speleers H.. Symbol-based multigrid methods for Galerkin B-spline isogeometric analysis. *SIAM Journal on Numerical Analysis.* 2017;:31–62.

20. Chan Jesse, Evans John A.. Multi-patch discontinuous Galerkin isogeometric analysis for wave propagation: Explicit time-stepping and efficient mass matrix inversion. *Computer Methods in Applied Mechanics and Engineering.* 2018;333:22–54.

21. Schaeuble Anne-Kathrin, Tkachuk Anton, Bischoff Manfred. Variationally consistent inertia templates for B-spline- and NURBS-based FEM: Inertia scaling and customization. *Computational Methods in Applied Mechanics and Engineering.* 2017;326:596–621.

22. Cottrell J A, Reali A, Bazilevs Y, Hughes T J R. Isogeometric analysis of structural vibrations. *Computer Methods in Applied Mechanics and Engineering.* 2006;195(41–43):5257—5296.

23. Hughes Thomas J.R., Evans John A., Reali Alessandro. Finite element and NURBS approximations of eigenvalue, boundary-value, and initial-value problems. *Computer Methods in Applied Mechanics and Engineering.* 2014;272:290–320.

24. Hughes T.J.R., Reali A., Sangalli G.. Duality and unified analysis of discrete approximations in structural dynamics and wave propagation: Comparison of p-method finite elements with k-method NURBS. *Computer Methods in Applied Mechanics and Engineering.* 2008;197(49):4104–4124.

25. Reali A.. An isogeometric analysis approach for the study of structural vibrations. *Journal of Earthquake Engineering.* 2006;10(1):1–30.

26. Bazilevs Y, Veiga L Beir Cottrell J A, Hughes T J R, Sangalli G. Isogeometric Analysis: Approximation, stability and error estimates for h-refined meshes.. *Mathematical Models and Methods in Applied Sciences.* 2006;16(7):1031–1090.

27. Cottrell J A, Hughes T J R, Bazilevs Y. *Isogeometric Analysis: Toward Integration of CAD and FEA*. John Wiley & Sons; 2009.

28. Piegel L A, Tiller W. *The NURBS Book (Monographs in Visual Communication).* Springer-Verlag; 2 ed.1997.

29. Borden Michael J., Scott Michael A., Evans John A., Hughes Thomas J. R.. Isogeometric finite element data structures based on Bézier extraction of NURBS. *International Journal for Numerical Methods in Engineering.* 2011;87(1-5):15–47.

30. Brivadis Ericka, Buffa Annalisa, Wohlmuth Barbara I, Wunderlich Linus. Isogeometric mortar methods. *Computer Methods in Applied Mechanics and Engineering.* 2015;284:292–319.

31. Seitz Alexander, Farah Philipp, Kremheller Johannes, Wohlmuth Barbara I, Wall Wolfgang A, Popp Alexander. Isogeometric dual mortar methods for computational contact mechanics. *Computer Methods in Applied Mechanics and Engineering.* 2016;301:259–280.

32. Dornisch W., Stöcklerb J., Müller R.. Dual and approximate dual basis functions for B-splines and NURBS – Comparison and application for an ef cient coupling of patches with the isogeometric mortar method. *Computer Methods in Applied Mechanics and Engineering.* 2017;316:449–496.

33. Scherer Karl, Schumaker Larry L.. A dual basis for L-Splines and applications. *Journal of Approximation Theory.* 1980;29(151–169).

34. Schumaker Larry L.. *Spline Functions: Basic Teory*. Cambridge University Press; 3rd ed.2007.

35. Lamichhane B P, Wohlmuth B I. Biorthogonal bases with local support and approximation properties. *Mathematics of Computation.* 2007;76(257):233–249.

36. Woźny Paweł. Construction of dual bases. *Journal of Computational and Applied Mathematics.* 2013;245:75–85.

37. Zou Z., Scott M. A., Borden M. J., Thomas D. C., Dornisch W., Brivadis E.. Isogeometric Bézier dual mortaring: Refineable higher-order spline dual bases and weakly continuous geometry. *Computer Methods in Applied Mechanics and Engineering.* 2018;.

38. Tkachuk Anton, Bischoff Manfred. Variational methods for selective mass scaling. *Computational Mechanics.* 2013;52:563–570.

39. Felippa Carlos A, Guo Qiong, Park Kwang-Chun. Mass Matrix Templates: General Description and 1D Examples. *Archives of Computational Methods in Engineering.* 2014;22(1):1–65.

40. Kolman Radek, Plešek Jiří, Červ Jan, Okrouhlík Miloslav, Pařík Petr. Temporal-spatial dispersion and stability analysis of finite element method in explicit elastodynamics. *International Journal for Numerical Methods in Engineering.* 2015;106(2):113–128.

41. Graff Karl F.. *Wave motion in elastic solids*. Dover Publications; 1975.

42. Wang Dongdong, Liu Wei, Zhang Hanjie. Novel higher order mass matrices for isogeometric structural vibration analysis. *Computer Methods in Applied Mechanics and Engineering.* 2013;260:92–108.

43. Wang Dongdong, Liu Wei, Zhang Hanjie. Superconvergent isogeometric free vibration analysis of Euler–Bernoulli beams and Kirchhoff plates with new higher order mass matrices. *Computer Methods in Applied Mechanics and Engineering.* 2015;286:230–267.

44. Wang Dongdong, Liang Qingwen, Wu Junchao. A quadrature-based superconvergent isogeometric frequency analysis with macro-integration cells and quadratic splines. *Computer Methods in Applied Mechanics and Engineering.* 2017;320:712 - 744.

45. Park K. C.. Practical aspects of numerical time integration. *Computers and Structures.* 1977;7:343–353.

46. Hulbert G, Chung J. Explicit time integration algorithms for structural dynamics with optimal numerical dissipation. *Computer Methods in Applied Mechanics and Engineering.* 1996;137:175–188.

47. Chang S. Y.. An explicit method with improved stability property. *International Journal for Numerical Methods in Engineering.* 2008;77(8):1100–1120.

48. Kolman R., Okrouhlík M., Berezovski A., Gabriel D., Kopačka J., Plešek J.. B-spline based finite element method in one-dimensional discontinuous elastic wave propagation. *Applied Mathematical Modelling.* 2017;46:382 - 395.

49. Kolman R., Plešek J., Okrouhlík M.. Complex wavenumber Fourier analysis of the B-spline based finite element method. *Wave Motion.* 2014;51(2):348 - 359.

50. *The standard NAFEMS benchmarks*. National Agency for Finite Element Methods & Standards. East Kilbride, Glasgow, U.K.; 1990.

51. Anděl Petr, Bastl Bohumír, Slabá Kristna. Parametrization of generalized NURBS volumes of revolution. *Engineering mechanics.* 2012;19(4):293–306.